

THE COS CGM COMPENDIUM V: THE DICHOTOMY OF O VI ASSOCIATED WITH LOW- AND HIGH-METALLICITY COOL GAS AT $z < 1$

SAMEER,¹ NICOLAS LEHNER,¹ J. CHRISTOPHER HOWK,¹ ANDREW J. FOX,^{2,3} JOHN M. O'MEARA,⁴ AND BENJAMIN D. OPPENHEIMER⁵

¹*Department of Physics and Astronomy, University of Notre Dame, Notre Dame, IN 46556, USA*

²*Space Telescope Science Institute, 3700 San Martin Drive, Baltimore, MD 21218, USA*

³*Department of Physics & Astronomy, Johns Hopkins University, 3400 N. Charles St., Baltimore, MD 21218, USA*

⁴*W.M. Keck Observatory 65-1120 Mamalahoa Highway, Kamuela, HI 96743, USA*

⁵*CASA, Department of Astrophysical and Planetary Sciences, University of Colorado, Boulder, CO 80309, USA*

ABSTRACT

We analyze the O VI content and kinematics for 126 H I-selected absorbers at $0.14 \lesssim z \lesssim 0.73$ for which the metallicities of their cool photoionized phase have been determined. We separate the absorbers into 100 strong Ly α forest systems (SLFSs with $15 \lesssim \log N(\text{H I}) < 16.2$) and 26 partial Lyman Limit systems (pLLSs with $16.2 \leq \log N(\text{H I}) < 17.2$). The sample is drawn from the COS CGM Compendium (CCC) and has O VI coverage in $S/N \geq 8$ *HST*/COS G130M/G160M QSO spectra, yielding a 2σ completeness level of $\log N(\text{O VI}) \geq 13.6$. The O VI detection rates differ substantially between low-metallicity (LM; $[\text{X}/\text{H}] \leq -1.4$) and high-metallicity (HM; $[\text{X}/\text{H}] > -1.4$) SLFSs, with 20% and 60% detection rates, respectively. The O VI detection frequency for the HM and LM pLLSs is, however, similar at $\sim 60\%$. The SLFSs and pLLSs without detected O VI are consistent with the absorbing gas being in a single phase, while those with O VI trace multiphase gas. We show that the O VI velocity widths and column densities have different distributions in LM and HM gas. We find a strong correlation between O VI column density and metallicity. The strongest ($\log N(\text{O VI}) \gtrsim 14$) and broadest O VI absorbers are nearly always associated with HM absorbers, while weaker O VI absorbers are found in both LM and HM absorbers. From comparisons with galaxy-selected and blind O VI surveys, we conclude absorbers with $\log N(\text{O VI}) \gtrsim 14$ most likely arise in the circumgalactic medium (CGM) of star-forming galaxies. Absorbers with weak O VI likely trace the extended CGM or intergalactic medium (IGM), while those without O VI likely originate in the IGM.

Keywords: circumgalactic medium — quasars: absorption lines — galaxies: halos — abundances

1. INTRODUCTION

The ionized gaseous halos surrounding galaxies play a crucial role in their evolution. These halos, a.k.a. the circumgalactic media (CGM), are important reservoirs of baryons and metals, harboring more than 50% of the baryonic and metal budget of the universe (e.g., Werk et al. 2014; Tumlinson et al. 2017; Péroux & Howk 2020). They regulate the processes of accretion and feedback in galaxies, which are necessary for galaxies to sustain star formation over cosmological timescales (e.g., Maller & Bullock 2004; Dekel & Birnboim 2006), but also to avoid forming more stars than observed (e.g., Kacprzak et al. 2008; Oppenheimer et al. 2010, 2012; Faucher-Giguère et al. 2011; Fumagalli et al. 2011). The growth and evolution of galaxies are driven by the exchange

of matter between them, their CGM, and the diffuse intergalactic medium (IGM) (e.g., Davé et al. 2012).

This exchange of matter can be probed by QSO absorption line systems, whose H I column density can serve as a metric of the overdensity (δ) of the gas (Schaye 2001). Absorbers with $\log N(\text{H I}) = 15\text{--}19$ fall between the diffuse IGM probed by the Ly α forest ($\log \delta < 1$, $\log N(\text{H I}) \lesssim 14.5$) and the galaxies that can be probed by damped Ly α absorbers ($\log N(\text{H I}) \gtrsim 20.3$). These absorbers at the interface between the IGM and galaxies comprise the strong Ly α forest systems (SLFSs; $\log N(\text{H I}) = 15\text{--}16.2$), the partial Lyman limit systems (pLLSs; $\log N(\text{H I}) = 16.2\text{--}17.2$), and the Lyman limit systems (LLSs; $\log N(\text{H I}) = 17.2\text{--}19$) following the nomenclature defined in Lehner et al. (2018) (hereafter CCC I). Studies of galaxies in QSO fields where these

absorbers have been observed show that indeed they often probe the CGM of galaxies (e.g., Steidel et al. 1995; Chen & Prochaska 2000; Cooper et al. 2021; Wilde et al. 2021; Berg et al. 2023). The BASIC survey (Berg et al. 2023) shows that while the metal-enriched pLLSs at $z \lesssim 1$ are indeed always associated with (relatively massive) galaxies, the very metal-poor pLLSs, on the other hand, can track a more diverse set of physical structures, including the CGM of galaxies, and also dense regions of the IGM devoid of any galaxies down to very low masses. The MAGG survey similarly shows that LLSs at $z \sim 3\text{--}4$ are either located in regions close to galaxies or likely in filaments of the IGM (Fumagalli et al. 2016; Lofthouse et al. 2020, 2023). While future and ongoing surveys will refine these findings, it is evident already that strong H I absorbers with $15 \lesssim \log N(\text{H I}) \lesssim 19$ probe a wide range of environments, especially for the low-metallicity population; the metallicity is a key diagnostic for deciphering the origins of the strong H I absorbers. In low- z simulations, absorbers with $\log N(\text{H I}) \gtrsim 15$ generally track the CGM of galaxies within the impact parameters of 300 kpc (e.g., Hafen et al. 2017; Weng et al. 2024). However, very high-resolution cosmological simulations of the IGM at $z \sim 3$ also show that LLSs can be found in small-scale, dense-cloud structures of the IGM that were not resolved in lower-resolution simulations (Mandelker et al. 2019, 2021).

Fumagalli et al. (2016) (and see also Wotta et al. 2016; Wotta et al. 2019—hereafter CCC II; Lehner et al. 2019—hereafter CCC III; Gibson et al. 2022) showed that the metallicity estimates in the (predominantly) ionized regions of the universe are less dependent on the ionization assumptions, such as the slope of the extreme ultraviolet background (EUVB), than other gas properties such as hydrogen density, size scale, or the total hydrogen column density, making metallicity a robust probe of the origin and chemical enrichment history of the gas associated with strong H I absorbers. For example, Gibson et al. (2022) find that the average uncertainty of inferred metallicities of lower-ionization gas only increased from 0.08 dex to 0.14 dex when switching from models with a fixed EUVB slope to those with slope varying over -2.0 to -1.4 for the KS19 ionizing background models (Khaire & Srianand 2019).

The strong H I absorbers (SLFSs, pLLSs, and LLSs) exhibit absorption in low ions (e.g., C II, Mg II, Si II), intermediate ions (e.g., O II, O III, Si III, C III), and sometimes O IV that have velocity profiles that are similar to the associated H I absorption profiles (CCC I).¹ All

these ions can also be in many cases modeled with a single-phase, photoionization model where the ionization is produced by the EUVB (e.g., Cooksey et al. 2008; Lehner et al. 2013; CCC II; CCC III; Zahedy et al. 2019), although in some cases (especially in the pLLS and LLS regimes), they may require more than a single ionization phase (e.g., Lehner et al. 2019; Haislmaier et al. 2021; Qu et al. 2022; Sameer et al. 2024). Some of these H I absorbers also have O VI absorption found at similar redshifts (especially, for absorbers $\log N(\text{H I}) \gtrsim 16$), and these photoionization models generally underestimate the amount of O VI at $z \lesssim 1$, implying that, when O VI is detected, the gas probed by strong H I absorbers must have multiple gas-phases. The reason is that the EUVB is typically not hard enough at $z \lesssim 1$ and the densities are not low enough to produce the O VI with the other ions in a single-phase photoionized gas for these absorbers (e.g., Cooksey et al. 2008; Lehner et al. 2009; Kacprzak et al. 2012; Crighton et al. 2013; Lehner et al. 2013; Savage et al. 2014—hereafter S14; Werk et al. 2016; Rosenwasser et al. 2018; Cooper et al. 2021; Haislmaier et al. 2021; Sameer et al. 2021, 2024; Zahedy et al. 2019). As these studies show, this does not necessarily mean that O VI always traces collisionally ionized gas. O VI can also be present in photoionized gas, but with much lower densities than in the gas probed by the bulk of the cool H I observed in these absorbers (e.g., S14; Muzahid et al. 2015; Werk et al. 2016; Rosenwasser et al. 2018; Haislmaier et al. 2021). This means the O VI must be produced in a different gas phase than the lower ions. The O VI velocity profiles in some instances also show a lack of kinematic correspondence with the H I; indicating that the O VI-bearing gas resides in a separate phase (e.g., Lehner et al. 2014; S14; Werk et al. 2016).

Owing to its high frequency of occurrence and high ionization state, O VI is therefore an important and complementary diagnostic of very low density cool photoionized gas and warm-hot, collisionally ionized gas (e.g., S14). Strong O VI absorbers with large column densities ($\log N(\text{O VI}) \gtrsim 14.5$) and velocity widths ($\Delta v(\text{O VI}) \gtrsim 100 \text{ km s}^{-1}$) have been directly identified in some instances with large-scale outflows from starburst galaxies (e.g., Grimes et al. 2009; Tripp et al. 2011; Muzahid et al. 2015; Rosenwasser et al. 2018). The CGM² survey (a galaxy-centric survey at $0.1 \lesssim z \lesssim 0.6$ of 52 galaxies with stellar masses of $\sim 3 \times 10^{10} M_{\odot}$) recently shows that O VI absorbers with $\log N(\text{O VI}) \gtrsim 14.3$ are nearly al-

ing ionization potentials between 15.04–24.38 eV, and intermediate ions (O II, O III, Si III, C III) having ionization potentials between 33.49–54.94 eV. O IV with an ionization potential of 77.41 eV, represents a higher ionization state.

¹ The separation between the low and intermediate ions is based on their ionization potentials, with low ions (C II, Mg II, Si II) hav-

ways found around star-forming galaxies (covering fraction $\gtrsim 90\%$), but rarely around passive galaxies (covering fraction $\lesssim 20\%$) with similar stellar or halo masses (Tchernyshyov et al. 2023; and see also Tumlinson et al. 2011, Tchernyshyov et al. 2022; hereafter T22), implying a CGM transformation when galaxies quench and a relationship between the star formation level in galaxy and the amount of O VI in its CGM. As for the low metallicity pLLSs and LLSs, weaker O VI absorbers have a wider range of origins, including the IGM, extended CGM or intragroup gas, or CGM of dwarf galaxies (e.g., Stocke et al. 2014, 2017; S14; T22; Tchernyshyov et al. 2023).

The investigation of the relationship between the metallicity of low ionization CGM gas with the properties of the O VI gas can lead to new and additional insights on the origins of the O VI absorbers and multiple gas phases of these absorbers. At $z < 1$, an earlier study of Fox et al. (2013) using a sample 23 H I-selected pLLSs shows a high-frequency rate of detection of O VI ($\sim 70\%$) and strongly hints that the strength of O VI absorption is correlated with the metallicity of the photoionized gas; with metal-poor pLLSs showing an absence of strong O VI with $\log N(\text{O VI}) \gtrsim 14.5$. At $z > 2$, the Keck Observatory Database of Ionized Absorption toward Quasars (KODIAQ; Lehner et al. 2014) survey led to a similar conclusion where the strongest O VI absorbers associated with $\log N(\text{H I}) \gtrsim 17$ absorbers were found in the highest metallicity systems (Lehner et al. 2014; Lehner 2017).² These two surveys have a relatively small sample size, with only about 5–10 metal-poor absorbers. Neither explores the O VI associated with lower column density SLFSs.

Here we revisit and expand the Fox et al. (2013) study with a much larger sample of absorbers drawn from the COS CGM Compendium survey (CCC, CCC I; CCC II; CCC III) that includes both pLLSs and SLFSs, spanning the redshift range of $0.14 \lesssim z \lesssim 0.73$. We also aim to understand the origins of the O VI properties in this H I-selected sample by comparing with several recent galaxy-centric and blind O VI surveys that were not available at the time of the Fox et al. survey (e.g., S14; T22). The CCC is a high-resolution survey of H I-selected absorbers at $z < 1$ that has focused so far on the metallicity of cool photoionized gas. The O VI-bearing gas in these absorbers was not detailed beyond basic measurements, except noting that the O VI could

not be reproduced by the same photoionization models that produce the lower ions in the pLLSs and LLSs (see Lehner et al. 2013). The H I-selection of the CCC survey eliminates any metallicity bias, allowing one to detect both high- and low-metallicity gas. It is also blind in terms of the presence of the O VI absorption that might be associated (or not) with the H I and lower ion absorption. This experiment with its selection criteria can be easily replicated in cosmological simulations for a comparison between theory and observations (e.g., CCC III, Lehner et al. 2022b). This H I-selection approach leads to a widely different distribution of the H I column densities (and as we will show of the O VI column density distribution as well) compared to blind O VI surveys where the absorbers have typically H I column densities of $\log N(\text{H I}) \lesssim 15$ (e.g., Danforth & Shull 2005; Tripp et al. 2008; Thom & Chen 2008a,b; Danforth et al. 2016).

Our paper is structured as follows. In Section 2, we describe the sample. In Section 3, we present our empirical approach to investigating the relationship between H I and O VI. Our main results are presented in Section 4 and discussed in Section 5. In Section 6, we summarize our main findings.

We adopt the notations μ , $\mu_{1/2}$, σ , σ_μ , and $\sigma_{\mu_{1/2}}$, to denote the mean, median, intrinsic scatter of the distribution, and measurement uncertainty on the mean and median, respectively. Throughout this work, we consider a p -value ≤ 0.05 (corresponding to a significance level of $\approx 2\sigma$) as the threshold for rejecting the null hypothesis and claiming statistical significance. In this study, we employed survival analysis techniques to handle the presence of upper limits in our data. Survival analysis methods independently do not account for measurement errors. To address this limitation, we implemented a Monte Carlo sampling approach in conjunction with survival analysis (e.g., Shy et al. 2022). We generated 1000 replicated datasets, where each measurement in the dataset was randomly drawn from an underlying distribution modeled as a Fechner distribution (Wallis 2014) or a Gaussian distribution, depending on the nature of uncertainties. The Fechner distribution is chosen to treat the asymmetric uncertainty associated with the measurements appropriately. We utilized the FANPLOT package (Abel 2015) in R to facilitate the modeling of the asymmetric uncertainty. We then performed the relevant statistical test (e.g., Kaplan-Meier estimator (KM) (Kaplan & Meier 1958), Akritas-Theil-Sen (ATS) (Akritas et al. 1995) test, log-rank test (Mantel et al. 1966), Anderson-Darling (AD) test (Scholz & Stephens 1987), Mann-Whitney U (MWU) test (Mann & Whitney 1947), or

² Owing to the cosmic evolution, low-metallicity gas is defined as $[X/H] \lesssim -2.4$ and $\lesssim -1.4$ at $2.2 \lesssim z \lesssim 3.5$ and $z \lesssim 1$, respectively (Lehner et al. 2022b; CCC III). Below these thresholds, it is very rare to find DLAs, but about 50% of the SLFSs, pLLSs, and LLSs are found at all redshifts surveyed so far.

Table 1. Number of spectra with O VI coverage

Sample	SLFSs	pLLSs	Total	$\langle z \rangle$	$[X/H]^a$
Entire	133	37	170	0.44	$-1.22^{+0.23}_{-0.11}$
Robust: $S/N \geq 8$	100	26	126	0.41	$-1.22^{+0.23}_{-0.11}$
HM: $S/N \geq 8$ & $[X/H] > -1.4$	64	18	82	0.40	$-0.76^{+0.15}_{-0.14}$
LM: $S/N \geq 8$ & $[X/H] \leq -1.4$	36	8	44	0.42	$-2.01^{+0.05}_{-0.25}$

NOTE—*a*: median metallicity and upper/lower bounds of the 95% confidence interval of the sample, which is determined using the KM estimator, accounting for the upper limits.

Kolmogorov-Smirnov (KS) test (Hodges 1958) on each of the 1000 datasets. The resulting distribution of the statistic of interest (e.g., mean or p-value) is summarized using its mean and standard deviation.

2. SAMPLE

CCC I assembled a sample of 222 H I-selected absorbers with $15.1 \lesssim \log N(\text{H I}) \lesssim 19$ at $z \lesssim 1$. The *HST*/COS G130M and/or G160M spectral data were retrieved from the HST Spectroscopic Legacy Archive (HSLA, Peebles et al. 2017) available at the Barbara A. Mikulski Archive for Space Telescopes (MAST). These data were uniformly analyzed to derive the column densities of H I and metal ions and atoms. As pointed out in CCC I, an additional 39 absorbers are available from earlier surveys (Lehner et al. 2013; Wotta et al. 2016). These additional absorbers were observed with *HST*/STIS E140M, *FUSE*, and *HST*/COS G140L; their column densities were not reassessed in CCC I.

We adopt the column densities for H I, C II, and C III from CCC I and the metallicities of the cool photoionized gas probed by the SLFSs and pLLSs from CCC III. As explained in CCC II and CCC III, the photoionization modeling of these absorbers was motivated by the empirical findings of CCC I that showed that the properties of the low (e.g., C II, Mg II) and intermediate (e.g., O II, C III) ions and H I in the SLFSs and pLLSs are characteristics of the gas being photoionized (and even in some cases O IV)³. The metallicity determination was

³ CCC III, as part of their analysis of the SLFSs, revisited the inclusion of O IV in the single-phase photoionization models (which was not included for the pLLSs in CCC II) and found that 12/17 SLFSs and 3/8 pLLSs could be modeled with the inclusion of O IV. The other absorbers must probe multiphase gas. As demonstrated in CCC III (see their Fig. 2) the metallicities derived with or without O IV in the photoionization models do not drastically change (on average, a 0.06 dex difference in the mean metallicity of the sample with and without O IV). In this work, we adopt the metal-

therefore done with a single-phase photoionization model using an MCMC technique that employs Bayesian statistics (see Cooper et al. 2015; Crighton et al. 2015; Fumagalli et al. 2016; Wotta et al. 2019; Lehner et al. 2019). The result is a posterior probability density function (PDF) for the metallicity of each absorber. This method also formally treats the lower and upper limits.

The signal-to-noise levels of the COS spectra are not high enough to pursue an unbiased survey of the metallicity at $z \lesssim 1$ in the more diffuse gas probed by weak H I absorbers with $\log N(\text{H I}) \gtrsim 15$, and this sets the lower limit on $\log N(\text{H I})$ for CCC and therefore for our sample. Two systems, the $z = 0.3905$ towards J020930.74-043826.2 and $z = 0.47404$ towards J154553.63+093620.5, have $\log N(\text{H I}) = 19$ and 18.2, respectively. Since there are only two LLSs with H I column with O VI information, we set the upper limit of $\log N(\text{H I}) = 17.2$ for our sample. Hence we consider only SLFSs and pLLSs in our analysis, totaling 171 absorbers with O VI coverage of at least one of the doublet transitions.⁴ To minimize the influence of non-informative upper limits, we created a robust sample adopting signal-to-noise $S/N \geq 8$ per resolution element near the O VI doublet, reducing the sample to 127 absorbers with O VI coverage and a sensitivity level of $\log N(\text{O VI}) \geq 13.6$ at the 2σ level.

We do not a priori exclude proximate absorbers, i.e., absorbers with small velocity separation from the back-

licities from CCC III since the same methodology was applied for all the SLFSs and pLLSs.

⁴ For two absorbers—the $z = 0.1385$ system toward PG1116+215 and the $z = 0.1671$ absorber toward PKS0405-123—the O VI information was not available in CCC III, as at these redshifts STIS and *FUSE* are required to determine $N(\text{H I})$. We maximize the number of pLLSs in our sample by adopting the H I column densities for these absorbers from Lehner et al. (2013) and use *FUSE* data for the estimation of the O VI properties.

ground QSO ($\Delta v < 3000 \text{ km s}^{-1}$), in our analysis, except for one case. They constitute a small percentage of our sample, with $\approx 8\%$ being proximate. CCC I showed that for all but one, their properties are quite similar to intervening absorbers. The exception is the absorber at $z = 0.470800$ toward the quasar J161916.54+334238.4, where there is extremely strong absorption of intermediate to high ions, and the O VI might even be saturated. This absorber also has strong absorption features of S VI, S V, S IV, not typically observed except in the proximity of a very hard ionizing source, implying that this particular absorber is not only a proximate but also an associated system. We, therefore, exclude this absorber, reducing our total sample to 126 absorbers; this is the primary sample for this paper (see Section 4.1). In Fig. 1, as an example, we present the apparent optical column density profiles for O VI, C II, C III, and H I for two closely redshift-separated absorbers from our sample. The complete set of $N_a(v)$ and normalized flux profiles for the entire sample of O VI absorbers is provided as online supplementary material. Each plot features a robustness flag (RF), where RF = 1 indicates the absorption system is part of the primary (robust) sample, and RF = 0 indicates it is not.

In Table 1, we summarize the numbers of H I-selected absorbers grouped in N_{HI} , metallicity, S/N groupings. The mean redshift and median metallicity, $[\text{X}/\text{H}]$, of these samples is also noted. For the remainder of the paper, except otherwise noted, we only consider the robust sample for our analysis and interpretation of the O VI associated with the H I-selected absorbers. We select a threshold of the metallicity at $[\text{X}/\text{H}] = -1.4$ following CCC II, which corresponds to the 2σ lower bound of the DLA metallicities at $z \lesssim 1$. The absorbers below this metallicity were defined in CCC II and CCC III as “very metal-poor” absorbers; here we simply refer to them as low-metal (LM) absorbers, and absorbers with $[\text{X}/\text{H}] > -1.4$ as high-metal (HM) absorbers.

LM absorbers are very rare for DLAs at $z \lesssim 1$, but are very common for lower H I column density absorbers with $\log N(\text{H I}) < 19$ (see CCC III). Low redshift DLAs typically trace the interstellar medium or extended gaseous disks of galaxies within approximately 20 kpc, as evidenced by the correlation between H I col-

umn density and impact parameter (e.g., Lehner et al. 2013; Berg et al. 2023; Weng et al. 2023). In contrast, lower H I column density absorbers (pLLSs and LLSs) are found over a wider range of impact parameters, typically beyond 20 kpc from galaxies.

3. KINEMATICS AND COLUMN DENSITY MEASUREMENTS

CCC I adopted the apparent optical depth (AOD) method (Savage & Sembach 1991) for estimating the column densities of the metal lines associated with the H I. We adopt the same method here to derive the properties of the O VI absorbers. In short, with this method, the absorption profiles are converted into apparent optical depth per unit velocity, $\tau_a(v) = \ln[F_c(v)/F_{\text{obs}}(v)]$, where $F_c(v)$ and $F_{\text{obs}}(v)$ are the modeled continuum and observed fluxes as a function of velocity. The AOD, $\tau_a(v)$, is related to the apparent column density per unit velocity, $N_a(v)$, through the relation $N_a(v) = 3.768 \times 10^{14} \tau_a(v)/(f\lambda) \text{ cm}^{-2} (\text{km s}^{-1})^{-1}$, where f is the oscillator strength of the transition and λ is the wavelength in Å. The total column density is obtained by integrating the profile over a pre-defined velocity interval, $N = \int_{v_{\text{min}}}^{v_{\text{max}}} N_a(v) dv$, where $[v_{\text{min}}, v_{\text{max}}]$ are the boundaries of the absorption. We computed the $N_a(v)$ -weighted average line centroids through the first moment of the AOD, $v_a = \int v N_a(v) dv / \int N_a(v) dv \text{ km s}^{-1}$. With the AOD method, both contamination and saturation can be determined using the prescriptions described in CCC I (see their Section 4.2).

Besides the velocity centroid and column density, we characterize the velocity width of absorption using the velocity interval that encloses the central 90% of the integrated AOD in the absorption line, Δv_{90} (Prochaska & Wolfe 1997). It is measured by integrating the absorption line between v_{min} and v_{max} , and finding the velocity difference between pixels at which 5% and 95% of the total apparent optical depth is attained. For a saturated line, we derive an upper limit to Δv_{90} for the true column density because saturation in the absorption line can lead to an underestimation of the true optical depth. We thus treat the measured Δv_{90} as an upper limit for saturated absorption.

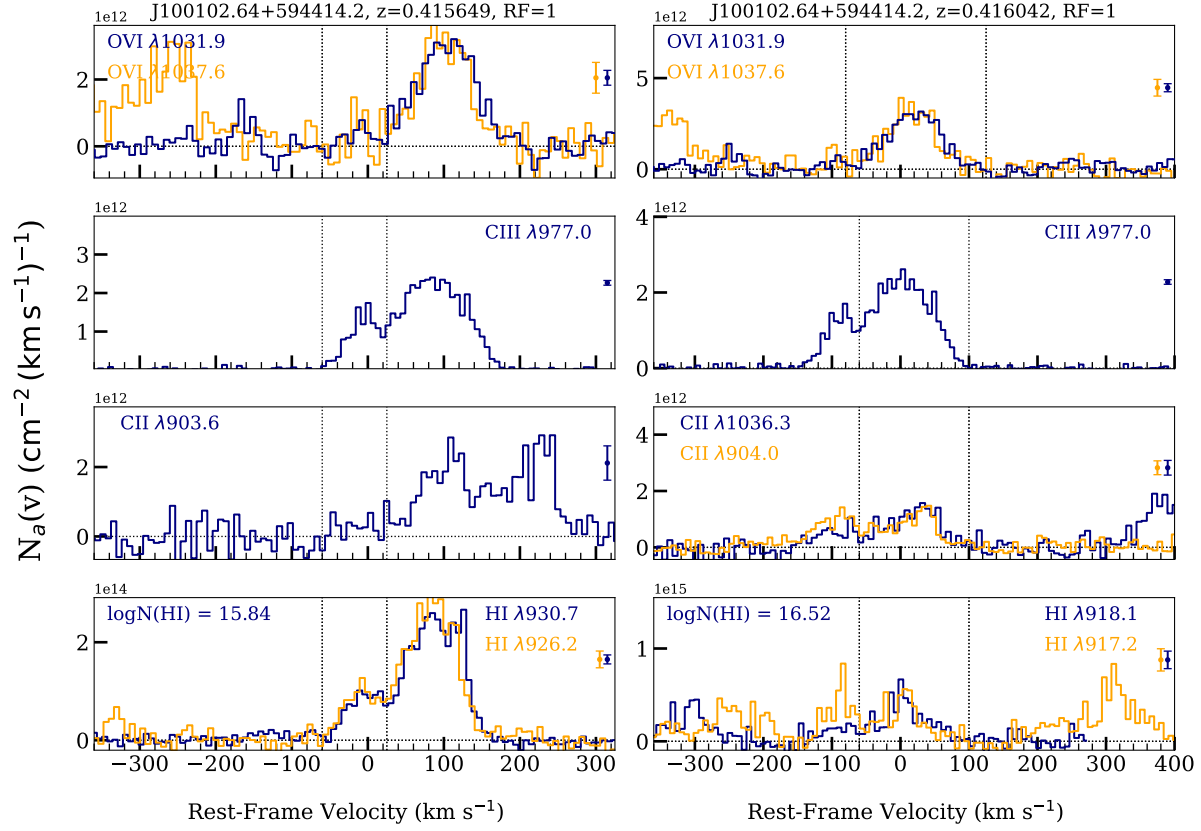


Figure 1. Apparent optical column density profiles for O VI, C II, C III, and HI, for two closely redshift-separated absorbers at $z = 0.415649$ (*left*) and 0.416042 (*right*) toward the quasar J100102.64+594414.2. These two absorbers are separated by 100 km s^{-1} . The integrated velocity ranges are indicated by two vertical lines in each panel. O VI is detected only at $z = 0.416042$. In this case, these are HM absorbers with a similar metallicity within 1σ . The average uncertainty on the data is indicated to the right in each of the panels. Each plot includes a robustness flag (RF) indicating whether the absorption system is part of the robust sample (RF = 1) or not (RF = 0). The profiles are binned by 3 pixels for display purposes.

Table 2. Properties of the O VI absorbers in the CCC survey

Target	z_{abs}	v_{min} (km s^{-1})	v_{max} (km s^{-1})	$\langle v \rangle$ (km s^{-1})	Δv_{90} (km s^{-1})	Δv_{90} (km s^{-1})	Δv_{90} (km s^{-1})	$\log N$ [cm^{-2}]	Detection	Flag	$\log N$ [cm^{-2}]	Detection	Flag	S/N	S/N
(1)	(2)	(3)	(4)	(5)	(6)	(7)	(8)	(9)	(10)	(11)	(12)	(13)	(14)	$\lambda 1031$	$\lambda 1037$
J000559.23+160948.9	0.3058	-100.0	40.0	-52.0 ± 8.8	...	46.9 ± 12.5	...	13.38 ^{+0.08} _{-0.10}	0	< 13.26	-1	21.6	-1	23.3	23.3
J000559.23+160948.9	0.3479	-50.0	20.0	-18.5 ± 1.0	-22.0 ± 1.9	58.1 ± 1.4	51.4 ± 2.6	13.99 ^{+0.02} _{-0.02}	0	13.97 ^{+0.04} _{-0.04}	0	21.0	0	17.4	17.4
J000559.23+160948.9	0.3662	-50.0	50.0	-3.3 ± 1.1	-0.3 ± 1.9	74.2 ± 1.6	82.5 ± 2.6	14.07 ^{+0.02} _{-0.02}	-3	14.02 ^{+0.03} _{-0.03}	0	21.5	0	27.8	27.8
J004222.29-103743.8	0.3161	-60.0	70.0	-4.4 ± 7.8	...	72.7 ± 11.1	...	13.97 ^{+0.09} _{-0.12}	0	< 13.84	-1	8.5	-1	8.9	8.9
J004705.89+031954.9	0.3139	-50.0	50.0	< 13.39	-1	< 13.69	-1	10.0	-1	9.6	9.6
J004705.89+031954.9	0.3143	-50.0	100.0	< 13.48	-1	< 13.77	-1	9.9	-1	9.8	9.8
J011013.14-021952.8	0.2272	-110.0	100.0	-24.6 ± 2.5	-13.6 ± 5.2	120.4 ± 3.5	134.1 ± 7.4	14.48 ^{+0.02} _{-0.02}	0	14.48 ^{+0.04} _{-0.05}	0	12.6	0	12.9	12.9
J011013.14-021952.8	0.5365	-20.0	40.0	4.1 ± 4.2	...	34.8 ± 6.0	...	13.59 ^{+0.11} _{-0.15}	0	< 13.39	-1	9.9	-1	11.9	11.9
J011013.14-021952.8	0.7190	-50.0	70.0	< 13.53	-1	< 13.87	-1	7.1	-1	6.6	6.6
J011016.25-021851.0	0.3991	-100.0	80.0	-8.6 ± 4.8	-4.6 ± 4.5	105.7 ± 6.7	125.3 ± 6.3	14.34 ^{+0.05} _{-0.05}	0	14.37 ^{+0.04} _{-0.05}	0	8.9	0	14.7	14.7
J011016.25-021851.0	0.5354	-50.0	40.0	< 13.44	-1	< 13.60	-1	8.8	-1	9.8	9.8
J011016.25-021851.0	0.7180	-70.0	70.0	-2.2 ± 6.5	-14.2 ± 9.8	80.9 ± 9.1	92.6 ± 13.9	14.31 ^{+0.08} _{-0.11}	0	14.54 ^{+0.14} _{-0.21}	-3	5.7	-3	5.4	5.4
J011623.04+142940.5	0.3338	-100.0	100.0	-9.3 ± 6.2	16.2 ± 12.5	137.2 ± 8.8	129.8 ± 17.7	14.33 ^{+0.05} _{-0.06}	0	14.36 ^{+0.09} _{-0.11}	0	7.8	0	7.6	7.6
J011935.69-282131.4	0.3483	-60.0	10.0	-4	< 13.09	-1	...	-1	24.2	24.2
J011935.69-282131.4	0.3487	-100.0	40.0	...	-34.4 ± 3.3	...	89.8 ± 4.7	...	-4	14.07 ^{+0.04} _{-0.04}	0	...	0	23.7	23.7
J012236.76-284321.3	0.3650	-45.0	80.0	18.2 ± 2.4	19.7 ± 5.3	76.5 ± 3.4	76.1 ± 7.5	13.98 ^{+0.03} _{-0.04}	0	13.93 ^{+0.06} _{-0.07}	0	15.9	0	15.0	15.0
J015513.20-450611.9	0.2260	-100.0	120.0	7.3 ± 2.1	10.2 ± 4.6	107.0 ± 3.0	113.5 ± 6.6	14.18 ^{+0.02} _{-0.02}	0	14.16 ^{+0.03} _{-0.04}	0	25.9	0	24.5	24.5
J020157.16-113233.1	0.3226	-50.0	50.0	< 12.89	-1	< 13.19	-1	19.4	-1	20.1	20.1
J020157.16-113233.1	0.3231	-40.0	25.0	-3.4 ± 3.1	-1.1 ± 2.4	52.6 ± 4.4	43.5 ± 3.4	13.27 ^{+0.07} _{-0.09}	0	13.70 ^{+0.06} _{-0.07}	-3	24.7	-3	23.1	23.1
J020157.16-113233.1	0.3234	-55.0	70.0	22.1 ± 1.6	...	87.5 ± 2.2	...	14.13 ^{+0.02} _{-0.02}	-3	< 13.29	-1	19.2	-1	20.3	20.3
J020157.16-113233.1	0.3245	-45.0	85.0	16.2 ± 1.4	16.5 ± 2.8	98.6 ± 2.0	104.6 ± 3.9	14.11 ^{+0.02} _{-0.02}	0	14.12 ^{+0.03} _{-0.04}	0	25.1	0	21.3	21.3
J023507.38-040205.6	0.3225	-40.0	40.0	-1.6 ± 2.9	...	66.1 ± 4.1	...	13.58 ^{+0.05} _{-0.06}	0	< 13.28	-1	18.7	-1	17.2	17.2
J023507.38-040205.6	0.7389	-80.0	100.0	12.4 ± 13.2	...	135.2 ± 18.6	...	14.14 ^{+0.11} _{-0.14}	0	...	-4	5.1	-4

Table 2 continued

Table 2 (continued)

Target	z_{abs}	v_{min} (km s^{-1})	v_{max} (km s^{-1})	$\langle v \rangle$ (km s^{-1})	$\langle v \rangle$ (km s^{-1})	Δv_{90} (km s^{-1})	Δv_{90} (km s^{-1})	Δv_{90} (km s^{-1})	$\log N$ [cm^{-2}]	Detection	Flag	$\log N$ [cm^{-2}]	Detection	Flag	S/N	S/N
(1)	(2)	(3)	(4)	(5)	(6)	(7)	(8)	(9)	(10)	(11)	(12)	(13)	(14)	(15)	(16)	(17)
J024337.66-303048.0	0.3037	-70.0	70.0	< 13.24	-1	< 13.58	-1	< 13.58	-1	13.4	13.6	
J024649.86-300741.3	0.3123	-60.0	100.0	25.6 ± 6.1	-5.2 ± 5.2	106.2 ± 8.6	149.2 ± 7.3	14.13 ^{+0.06} _{-0.07}	0	14.68 ^{+0.05} _{-0.06}	-3	14.68 ^{+0.05} _{-0.06}	-3	9.1	9.1	
J024649.86-300741.3	0.3359	-50.0	70.0	< 13.44	-1	< 13.74	-1	< 13.74	-1	9.4	8.7	
J035128.56-142908.0	0.3285	-70.0	100.0	-0.9 ± 11.6	...	92.3 ± 16.3	...	13.57 ^{+0.10} _{-0.12}	0	< 13.54	-1	< 13.54	-1	14.8	13.9	
J035128.56-142908.0	0.3569	-160.0	120.0	-13.2 ± 2.0	-23.2 ± 4.0	83.2 ± 2.8	159.5 ± 5.7	14.91 ^{+0.04} _{-0.04}	-3	14.69 ^{+0.03} _{-0.03}	0	14.69 ^{+0.03} _{-0.03}	0	13.5	13.7	
J035128.56-142908.0	0.3572	0.0	70.0	-4	< 13.34	-1	< 13.34	-1	...	13.7	
J035128.56-142908.0	0.4398	-100.0	100.0	-13.6 ± 7.1	9.6 ± 11.4	81.6 ± 10.0	96.0 ± 16.1	13.94 ^{+0.06} _{-0.06}	0	14.00 ^{+0.08} _{-0.10}	0	14.00 ^{+0.08} _{-0.10}	0	15.2	14.8	
J040148.98-054056.5	0.2195	-50.0	140.0	42.3 ± 3.2	35.9 ± 5.7	136.0 ± 4.6	127.9 ± 8.1	14.54 ^{+0.03} _{-0.03}	0	14.48 ^{+0.05} _{-0.05}	0	14.48 ^{+0.05} _{-0.05}	0	10.4	10.5	
J040148.98-054056.5	0.3238	-70.0	70.0	< 13.45	-1	< 13.75	-1	< 13.75	-1	9.2	9.4	
J040748.42-121136.3	0.1672	-125.0	95.0	-34.1 ± 0.4	-31.2 ± 1.1	149.2 ± 0.5	149.1 ± 1.6	14.63 ^{+0.00} _{-0.00}	0	14.63 ^{+0.01} _{-0.01}	0	14.63 ^{+0.01} _{-0.01}	0	72.2	59.5	
J040748.42-121136.3	0.3607	-30.0	30.0	0.3 ± 2.5	...	45.1 ± 3.5	...	12.81 ^{+0.07} _{-0.08}	0	...	-4	...	-4	56.1	...	
J044011.90-524818.0	0.3279	-80.0	80.0	< 13.18	-1	< 13.49	-1	< 13.49	-1	16.3	16.0	
J044011.90-524818.0	0.6150	-120.0	135.0	8.9 ± 2.7	1.7 ± 4.3	178.7 ± 3.8	171.5 ± 6.1	14.84 ^{+0.02} _{-0.02}	0	14.89 ^{+0.03} _{-0.03}	0	14.89 ^{+0.03} _{-0.03}	0	10.8	10.8	
J044011.90-524818.0	0.6157	-20.0	80.0	16.0 ± 5.3	...	72.8 ± 7.5	...	13.85 ^{+0.07} _{-0.09}	0	< 13.68	-1	< 13.68	-1	9.3	10.0	
J055224.49-640210.7	0.3451	-25.0	25.0	...	-2.1 ± 3.0	...	42.8 ± 4.3	< 12.67	-1	13.40 ^{+0.09} _{-0.11}	-3	13.40 ^{+0.09} _{-0.11}	-3	26.4	23.4	
J055224.49-640210.7	0.4461	-65.0	65.0	-0.6 ± 3.5	-7.6 ± 7.5	81.9 ± 5.0	81.1 ± 10.6	13.66 ^{+0.04} _{-0.05}	0	13.64 ^{+0.08} _{-0.10}	0	13.64 ^{+0.08} _{-0.10}	0	24.6	25.9	
J063546.49-751616.8	0.4175	-50.0	95.0	16.9 ± 1.5	24.1 ± 3.1	98.1 ± 2.1	112.7 ± 4.3	14.17 ^{+0.02} _{-0.02}	0	14.14 ^{+0.03} _{-0.03}	0	14.14 ^{+0.03} _{-0.03}	0	23.4	22.7	
J063546.49-751616.8	0.4528	-20.0	100.0	41.0 ± 4.1	...	80.9 ± 5.8	...	13.63 ^{+0.05} _{-0.06}	0	< 13.30	-1	< 13.30	-1	20.1	18.9	
J063546.49-751616.8	0.4685	-40.0	80.0	8.6 ± 3.7	15.5 ± 7.1	80.0 ± 5.2	86.9 ± 10.0	13.69 ^{+0.05} _{-0.05}	0	13.66 ^{+0.08} _{-0.10}	0	13.66 ^{+0.08} _{-0.10}	0	19.5	19.0	
J071950.89+742757.0	0.3777	-40.0	70.0	9.1 ± 3.4	...	69.4 ± 4.8	...	13.77 ^{+0.05} _{-0.05}	0	< 13.61	-1	< 13.61	-1	15.7	12.2	
J075112.30+291938.3	0.4318	-60.0	80.0	13.2 ± 3.8	6.0 ± 5.3	89.7 ± 5.4	88.9 ± 7.4	13.52 ^{+0.04} _{-0.05}	0	13.76 ^{+0.05} _{-0.06}	-3	13.76 ^{+0.05} _{-0.06}	-3	26.1	33.9	
J075112.30+291938.3	0.4945	-30.0	50.0	4.4 ± 6.2	...	57.2 ± 8.7	...	13.02 ^{+0.10} _{-0.14}	0	...	-4	...	-4	29.6	...	
J080908.13+461925.6	0.6191	-90.0	90.0	10.0 ± 4.5	1.5 ± 3.2	204.2 ± 6.4	92.5 ± 4.5	15.08 ^{+0.06} _{-0.07}	-3	14.74 ^{+0.04} _{-0.04}	0	14.74 ^{+0.04} _{-0.04}	0	10.5	10.8	
J084349.47+411741.6	0.5335	-40.0	40.0	< 13.63	-1	< 13.91	-1	< 13.91	-1	5.6	6.3	
J084349.47+411741.6	0.5411	-40.0	40.0	9.0 ± 7.4	...	76.7 ± 10.4	...	13.85 ^{+0.12} _{-0.18}	0	< 13.85	-1	< 13.85	-1	6.2	5.9	

Table 2 continued

Table 2 (continued)

Target	z_{abs}	v_{min} (km s^{-1})	v_{max} (km s^{-1})	$\langle v \rangle$ (km s^{-1})	$\langle v \rangle$ (km s^{-1})	Δv_{90} (km s^{-1})	Δv_{90} (km s^{-1})	Δv_{90} (km s^{-1})	$\log N$ [cm^{-2}]	Detection	Flag	$\log N$ [cm^{-2}]	Detection	Flag	S/N	S/N
(1)	(2)	(3)	(4)	(5)	(6)	(7)	(8)	(9)	(10)	(11)	(12)	(13)	(14)	(15)	(16)	(17)
J084349.47+411741.6	0.5437	-30.0	40.0	2.5 ± 4.7	...	48.5 ± 6.7	...	$13.91^{+0.11}_{-0.15}$	0	< 13.82	-1	< 13.82	-1	6.2	5.9	
J091440.38+282330.6	0.2442	-90.0	70.0	-18.6 ± 4.8	-17.4 ± 7.4	105.2 ± 6.8	111.6 ± 10.4	$14.44^{+0.05}_{-0.06}$	0	$14.37^{+0.07}_{-0.09}$	0	$14.37^{+0.07}_{-0.09}$	0	7.5	8.5	
J091440.38+282330.6	0.5995	-70.0	70.0	< 13.61	-1	< 13.91	-1	< 13.91	-1	7.4	7.0	
J092554.44+453544.5	0.3096	-50.0	50.0	< 13.12	-1	< 13.39	-1	< 13.39	-1	14.9	15.6	
J093518.19+020415.5	0.3547	-50.0	50.0	< 13.61	-1	< 13.89	-1	< 13.89	-1	6.4	6.7	
J093603.88+320709.3	0.3904	-60.0	60.0	< 13.97	-1	...	-4	...	-4	4.0	...	
J094331.61+053131.4	0.2290	-50.0	50.0	< 13.50	-1	< 14.03	-1	< 14.03	-1	8.3	5.6	
J094331.61+053131.4	0.3546	-60.0	40.0	< 13.61	-1	< 13.90	-1	< 13.90	-1	6.6	6.8	
J094331.61+053131.4	0.3549	-40.0	40.0	< 13.53	-1	< 13.84	-1	< 13.84	-1	6.7	6.8	
J100102.64+594414.2	0.4156	-60.0	25.0	< 13.05	-1	< 13.37	-1	< 13.37	-1	15.0	15.5	
J100102.64+594414.2	0.4160	-80.0	125.0	18.8 ± 2.3	14.7 ± 4.1	121.1 ± 3.2	127.7 ± 5.8	$14.46^{+0.02}_{-0.02}$	0	$14.45^{+0.03}_{-0.04}$	0	$14.45^{+0.03}_{-0.04}$	0	15.5	16.4	
J100110.20+291137.5	0.5565	-40.0	90.0	25.4 ± 5.9	-8.1 ± 7.2	75.6 ± 8.3	90.9 ± 10.2	$14.37^{+0.11}_{-0.14}$	0	$14.85^{+0.09}_{-0.12}$	-3	$14.85^{+0.09}_{-0.12}$	-3	5.7	6.0	
J100535.25+013445.5	0.4185	-60.0	60.0	-7.9 ± 7.7	...	90.7 ± 10.8	...	$13.39^{+0.09}_{-0.11}$	0	< 13.38	-1	< 13.38	-1	19.2	18.6	
J100535.25+013445.5	0.4197	-40.0	40.0	< 12.94	-1	< 13.28	-1	< 13.28	-1	18.7	18.6	
J100902.06+071343.8	0.3372	-65.0	40.0	< 13.52	-1	< 13.84	-1	< 13.84	-1	8.1	7.6	
J100902.06+071343.8	0.3554	-50.0	25.0	-13.2 ± 4.0	-12.6 ± 4.6	59.8 ± 5.6	57.6 ± 6.6	$14.57^{+0.15}_{-0.24}$	-3	$14.25^{+0.10}_{-0.12}$	0	$14.25^{+0.10}_{-0.12}$	0	7.3	6.1	
J101622.60+470643.3	0.2638	-60.0	45.0	-4	< 13.97	-1	< 13.97	-1	...	5.4	
J101622.60+470643.3	0.4322	-62.0	52.0	< 13.51	-1	< 13.80	-1	< 13.80	-1	8.7	8.0	
J101622.60+470643.3	0.6647	-77.0	77.0	< 13.84	-1	< 14.16	-1	< 14.16	-1	5.1	4.9	
J101622.60+470643.3	0.7278	-55.0	55.0	< 14.06	-1	< 14.40	-1	< 14.40	-1	3.1	3.0	
J104117.16+061016.9	0.6544	-20.0	40.0	< 13.26	-1	< 13.60	-1	< 13.60	-1	8.6	8.3	
J104117.16+061016.9	0.6551	-50.0	30.0	< 13.38	-1	< 13.69	-1	< 13.69	-1	8.6	8.3	
J104117.16+061016.9	0.6554	-36.0	50.0	< 13.39	-1	< 13.70	-1	< 13.70	-1	8.5	8.4	
J105945.24+144143.0	0.4658	-60.0	50.0	< 13.21	-1	< 13.55	-1	< 13.55	-1	13.2	12.9	
J105945.24+144143.0	0.5765	-60.0	80.0	21.6 ± 7.7	...	95.1 ± 10.9	...	$13.91^{+0.08}_{-0.10}$	0	< 13.74	-1	< 13.74	-1	8.5	8.9	

Table 2 continued

Table 2 (continued)

Target	z_{abs}	v_{min} (km s^{-1})	v_{max} (km s^{-1})	$\langle v \rangle$ (km s^{-1})	$\langle v \rangle$ (km s^{-1})	Δv_{90} (km s^{-1})	Δv_{90} (km s^{-1})	Δv_{90} (km s^{-1})	$\log N$ [cm^{-2}]	Detection	Flag	$\log N$ [cm^{-2}]	Detection	Flag	S/N	S/N
(1)	(2)	(3)	(4)	(5)	(6)	(7)	(8)	(9)	(10)	(11)	(12)	(13)	(14)	(15)	(16)	(17)
J105956.14+121151.1	0.3324	-60.0	60.0	< 13.43	-1	< 13.79	-1	9.1	9.1	8.6
J110047.85+104613.2	0.4151	-65.0	65.0	< 13.91	-1	...	-4	4.1	4.1
J110539.79+342534.3	0.2388	-60.0	65.0	1.4 ± 1.6	0.4 ± 1.7	105.2 ± 2.3	77.2 ± 2.4	14.62 ^{+0.02} _{-0.02}	-3	14.59 ^{+0.03} _{-0.03}	0	13.9	13.9	13.8
J111132.20+554725.9	0.6175	-40.0	75.0	< 13.24	-1	< 13.62	-1	12.0	12.0	11.5
J111132.20+554725.9	0.6827	-60.0	20.0	< 13.22	-1	...	-4	10.6	10.6
J111239.11+353928.2	0.2465	-50.0	50.0	-4	< 13.86	-1	6.3
J111507.65+023757.5	0.3692	-40.0	30.0	-7.8 ± 3.9	...	57.2 ± 5.5	...	13.78 ^{+0.09} _{-0.11}	0	< 13.61	-1	8.9	8.9	8.9
J111754.23+263416.6	0.3520	-40.0	50.0	6.4 ± 6.8	-6.3 ± 3.2	77.7 ± 9.7	63.9 ± 4.5	13.68 ^{+0.11} _{-0.14}	0	14.37 ^{+0.06} _{-0.07}	-3	9.3	9.3	9.6
J111754.23+263416.6	0.3523	-30.0	60.0	...	5.1 ± 7.8	...	90.0 ± 11.0	< 13.37	-1	13.91 ^{+0.11} _{-0.15}	0	9.3	9.3	9.5
J111908.59+211918.0	0.1385	-95.0	95.0	7.9 ± 2.9	6.8 ± 6.8	91.9 ± 4.1	114.9 ± 9.6	13.80 ^{+0.02} _{-0.03}	0	13.82 ^{+0.06} _{-0.06}	0	38.6	38.6	36.7
J112553.78+591021.6	0.5575	-60.0	60.0	< 13.54	-1	< 13.76	-1	7.3	7.3	9.1
J112553.78+591021.6	0.5582	-60.0	20.0	-19.3 ± 6.4	...	75.8 ± 9.1	...	13.76 ^{+0.13} _{-0.18}	0	< 13.67	-1	6.9	6.9	9.3
J112553.78+591021.6	0.5585	-20.0	60.0	-4	< 13.72	-1	8.4
J112553.78+591021.6	0.6784	-65.0	65.0	< 13.40	-1	< 13.72	-1	9.6	9.6	9.2
J113457.71+255527.8	0.4320	-60.0	30.0	-17.0 ± 4.9	...	67.5 ± 6.9	...	13.77 ^{+0.08} _{-0.10}	0	< 13.80	-1	10.6	10.6	8.3
J113457.71+255527.8	0.4323	-40.0	70.0	< 13.34	-1	< 13.93	-1	11.0	11.0	8.3
J113910.70-135044.0	0.3195	-75.0	40.0	-18.6 ± 2.0	-22.3 ± 3.8	85.7 ± 2.9	78.9 ± 5.4	14.02 ^{+0.03} _{-0.03}	0	14.00 ^{+0.05} _{-0.06}	0	17.8	17.8	17.5
J113956.98+654749.1	0.3257	-75.0	80.0	7.1 ± 1.5	3.9 ± 3.2	85.4 ± 2.2	78.3 ± 4.5	13.96 ^{+0.02} _{-0.02}	0	13.99 ^{+0.03} _{-0.04}	0	35.2	35.2	36.8
J113956.98+654749.1	0.5279	-60.0	10.0	-19.6 ± 5.9	...	49.0 ± 8.4	...	13.08 ^{+0.11} _{-0.16}	0	...	-4	21.3	21.3
J115120.46+543733.0	0.2525	-110.0	140.0	6.0 ± 1.9	17.3 ± 4.9	125.2 ± 2.7	131.2 ± 6.9	14.34 ^{+0.01} _{-0.01}	0	14.35 ^{+0.03} _{-0.03}	0	25.0	25.0	18.5
J115120.46+543733.0	0.6886	-60.0	60.0	< 13.19	-1	< 13.44	-1	13.6	13.6	13.9
J120158.75-135459.9	0.4094	-90.0	75.0	< 13.74	-1	< 14.08	-1	6.0	6.0	5.8
J121430.55+082508.1	0.3247	-40.0	60.0	< 13.36	-1	< 13.72	-1	9.6	9.6	9.3
J121430.55+082508.1	0.3838	-100.0	100.0	< 13.59	-1	< 13.93	-1	8.3	8.3	7.3
J121640.56+071224.3	0.3824	-40.0	60.0	...	14.9 ± 5.9	...	81.6 ± 8.4	...	-4	14.23 ^{+0.09} _{-0.12}	0	6.5

Table 2 continued

Table 2 (continued)

Target	z_{abs}	v_{min} (km s^{-1})	v_{max} (km s^{-1})	$\langle v \rangle$ (km s^{-1})	$\langle v \rangle$ (km s^{-1})	Δv_{90} (km s^{-1})	Δv_{90} (km s^{-1})	Δv_{90} (km s^{-1})	$\log N$ [cm^{-2}]	Detection	Flag	$\log N$ [cm^{-2}]	Detection	Flag	S/N	S/N
(1)	(2)	(3)	(4)	(5)	(6)	(7)	(8)	(9)	(10)	(11)	(12)	(13)	(14)	(15)	(16)	(17)
J121920.93+063838.5	0.2823	-25.0	90.0	15.2 ± 3.6	16.5 ± 8.1	81.5 ± 5.1	67.7 ± 11.4	13.63 ^{+0.10} _{-0.12}	0	13.63 ^{+0.10} _{-0.12}	0	21.8	21.2	0	21.8	21.2
J122317.79+092306.9	0.3795	-50.0	40.0	< 13.32	-1	...	-4	9.8	...	-4	9.8	...
J122454.44+212246.3	0.3784	-80.0	80.0	1.5 ± 2.6	-6.6 ± 4.7	88.5 ± 3.6	121.1 ± 6.6	14.05 ^{+0.03} _{-0.03}	0	14.29 ^{+0.03} _{-0.04}	-3	17.6	17.5	-3	17.6	17.5
J122454.44+212246.3	0.4208	-40.0	20.0	-4	< 12.98	-1	...	29.7	-1	...	29.7
J122454.44+212246.3	0.4214	-60.0	60.0	-9.8 ± 2.9	-10.4 ± 4.5	120.1 ± 4.1	67.3 ± 6.4	13.89 ^{+0.02} _{-0.02}	-3	13.75 ^{+0.05} _{-0.06}	0	29.9	30.3	0	29.9	30.3
J122512.93+121835.7	0.3250	-100.0	100.0	< 13.53	-1	< 13.88	-1	9.7	9.2	-1	9.7	9.2
J123304.05-003134.1	0.3188	-160.0	100.0	-34.0 ± 2.5	-44.0 ± 5.0	159.4 ± 3.6	158.6 ± 7.0	14.70 ^{+0.02} _{-0.02}	0	14.66 ^{+0.03} _{-0.03}	0	12.1	12.2	0	12.1	12.2
J123335.07+475800.4	0.2849	-60.0	60.0	0.3 ± 5.3	...	54.3 ± 7.5	...	13.93 ^{+0.08} _{-0.09}	0	< 13.73	-1	9.1	9.9	-1	9.1	9.9
J124154.02+572107.3	0.2179	-100.0	40.0	4.2 ± 2.1	6.6 ± 4.0	64.6 ± 3.0	71.2 ± 5.6	14.51 ^{+0.03} _{-0.04}	0	14.52 ^{+0.04} _{-0.05}	0	12.3	11.2	0	12.3	11.2
J124511.26+335610.1	0.5567	-60.0	60.0	-4	< 13.85	-1	...	5.6	-1	...	5.6
J124511.26+335610.1	0.5876	-50.0	50.0	< 13.42	-1	< 13.72	-1	9.8	9.2	-1	9.8	9.2
J124511.26+335610.1	0.6449	-70.0	70.0	< 13.52	-1	< 13.84	-1	7.6	8.2	-1	7.6	8.2
J124511.26+335610.1	0.6889	-60.0	25.0	-4	< 13.73	-1	...	7.4	-1	...	7.4
J124511.26+335610.1	0.6894	-60.0	25.0	-4	< 13.73	-1	...	7.4	-1	...	7.4
J124511.26+335610.1	0.7130	-40.0	50.0	8.8 ± 3.4	13.6 ± 10.8	68.6 ± 4.8	84.6 ± 15.3	14.31 ^{+0.06} _{-0.07}	0	14.55 ^{+0.17} _{-0.29}	-3	6.1	5.1	-3	6.1	5.1
J125846.65+242739.1	0.2262	-100.0	100.0	< 13.54	-1	< 13.84	-1	9.5	10.0	-1	9.5	10.0
J130429.02+311308.2	0.3099	-11.0	100.0	40.5 ± 2.4	35.0 ± 4.0	86.6 ± 3.4	86.0 ± 5.7	14.29 ^{+0.04} _{-0.04}	0	14.30 ^{+0.06} _{-0.06}	0	11.2	10.8	0	11.2	10.8
J130451.40+245445.9	0.2763	-75.0	75.0	< 13.43	-1	< 13.71	-1	11.0	10.7	-1	11.0	10.7
J133045.15+281321.5	0.2755	-80.0	90.0	7.9 ± 4.2	4.1 ± 7.9	102.6 ± 6.0	108.7 ± 11.1	14.29 ^{+0.05} _{-0.05}	0	14.28 ^{+0.07} _{-0.09}	0	9.3	9.7	0	9.3	9.7
J134100.78+412314.0	0.3488	-85.0	95.0	-3.2 ± 1.5	0.7 ± 2.7	96.7 ± 2.1	96.3 ± 3.8	14.52 ^{+0.02} _{-0.02}	0	14.51 ^{+0.03} _{-0.03}	0	14.7	14.3	0	14.7	14.3
J134100.78+412314.0	0.6208	-100.0	50.0	-0.5 ± 3.9	-21.1 ± 3.3	105.6 ± 5.6	133.1 ± 4.6	14.35 ^{+0.04} _{-0.05}	0	15.06 ^{+0.06} _{-0.06}	-3	9.5	7.8	-3	9.5	7.8
J134100.78+412314.0	0.6214	-80.0	130.0	-7.5 ± 3.2	-17.6 ± 2.6	158.1 ± 4.6	150.7 ± 3.7	14.95 ^{+0.05} _{-0.05}	0	14.99 ^{+0.02} _{-0.02}	0	11.2	12.2	0	11.2	12.2
J134100.78+412314.0	0.6861	-60.0	150.0	46.2 ± 2.1	53.4 ± 3.5	101.5 ± 3.0	101.1 ± 4.9	14.70 ^{+0.03} _{-0.03}	-2	14.75 ^{+0.03} _{-0.04}	-2	11.0	11.1	-2	11.0	11.1
J134447.55+554656.8	0.4042	-75.0	50.0	< 13.67	-1	...	-4	4.6	...	-4	4.6	...
J135726.26+043541.3	0.6102	-40.0	75.0	6.5 ± 2.4	-3.2 ± 4.0	79.9 ± 3.4	70.3 ± 5.6	14.41 ^{+0.04} _{-0.05}	0	14.89 ^{+0.09} _{-0.11}	-3	8.6	8.1	-3	8.6	8.1

Table 2 continued

Table 2 (continued)

Target	z_{abs}	v_{min} (km s^{-1})	v_{max} (km s^{-1})	$\langle v \rangle$ (km s^{-1})	$\langle v \rangle$ (km s^{-1})	Δv_{90} (km s^{-1})	Δv_{90} (km s^{-1})	Δv_{90} (km s^{-1})	$\log N$ [cm^{-2}]	Detection	Flag	$\log N$ [cm^{-2}]	Detection	Flag	S/N	S/N
(1)	(2)	(3)	(4)	(5)	(6)	(7)	(8)	(9)	(10)	(11)	(12)	(13)	(14)	(15)	(16)	(17)
J140732.25+550725.4	0.2433	-75.0	75.0	< 13.36	-1	< 13.60	-1	< 13.60	-1	< 13.60	11.8	12.4
J140732.25+550725.4	0.2469	-50.0	50.0	< 13.29	-1	< 13.43	-1	< 13.43	-1	< 13.43	12.3	14.6
J140923.90+261820.9	0.5749	-50.0	100.0	< 13.05	-1	< 13.27	-1	< 13.27	-1	< 13.27	21.5	20.7
J140923.90+261820.9	0.5996	-50.0	40.0	-8.7 ± 1.2	4.4 ± 2.0	80.2 ± 1.6	95.0 ± 2.8	13.99 ^{+0.02} _{-0.02}	0	14.10 ^{+0.03} _{-0.03}	-3	14.10 ^{+0.03} _{-0.03}	-3	14.10 ^{+0.03} _{-0.03}	21.2	22.8
J140923.90+261820.9	0.6827	-85.0	85.0	3.8 ± 2.4	-5.6 ± 4.9	89.1 ± 3.4	113.9 ± 6.9	14.09 ^{+0.02} _{-0.02}	0	14.05 ^{+0.04} _{-0.05}	0	14.05 ^{+0.04} _{-0.05}	0	14.05 ^{+0.04} _{-0.05}	20.6	20.7
J141038.39+230447.1	0.3498	-20.0	40.0	11.2 ± 2.6	14.0 ± 5.9	45.2 ± 3.6	76.8 ± 8.4	13.83 ^{+0.07} _{-0.09}	0	14.09 ^{+0.08} _{-0.10}	-3	14.09 ^{+0.08} _{-0.10}	-3	14.09 ^{+0.08} _{-0.10}	9.7	9.5
J141038.39+230447.1	0.3510	-50.0	55.0	< 13.40	-1	< 13.71	-1	< 13.71	-1	< 13.71	9.8	9.4
J141038.39+230447.1	0.5351	-20.0	75.0	23.8 ± 4.5	...	76.7 ± 6.4	...	13.73 ^{+0.07} _{-0.09}	0	< 13.68	-1	< 13.68	-1	< 13.68	12.4	7.7
J141910.20+420746.9	0.2890	-80.0	80.0	9.3 ± 3.8	-6.0 ± 7.6	101.4 ± 5.3	100.9 ± 10.8	14.51 ^{+0.05} _{-0.06}	0	14.46 ^{+0.08} _{-0.10}	0	14.46 ^{+0.08} _{-0.10}	0	14.46 ^{+0.08} _{-0.10}	8.1	7.1
J141910.20+420746.9	0.4256	-70.0	10.0	-27.9 ± 5.3	...	60.4 ± 7.5	...	13.73 ^{+0.10} _{-0.13}	0	< 13.74	-1	< 13.74	-1	< 13.74	8.8	8.0
J141910.20+420746.9	0.5221	-100.0	100.0	< 13.76	-1	< 14.08	-1	< 14.08	-1	< 14.08	5.9	5.3
J141910.20+420746.9	0.5346	-40.0	50.0	< 13.79	-1	< 14.15	-1	< 14.15	-1	< 14.15	4.5	4.4
J141910.20+420746.9	0.6083	-30.0	60.0	< 13.75	-1	< 14.04	-1	< 14.04	-1	< 14.04	4.7	4.9
J142735.59+263214.6	0.3661	0.0	105.0	35.8 ± 5.9	55.0 ± 5.4	112.3 ± 8.3	88.6 ± 7.6	14.74 ^{+0.10} _{-0.12}	-3	14.38 ^{+0.08} _{-0.10}	0	14.38 ^{+0.08} _{-0.10}	0	14.38 ^{+0.08} _{-0.10}	5.1	6.1
J142859.03+322506.8	0.3823	-20.0	80.0	23.9 ± 4.9	...	56.7 ± 6.9	...	13.79 ^{+0.08} _{-0.09}	0	...	-4	...	-4	...	10.0	...
J143511.53+360437.2	0.3730	-60.0	60.0	< 13.46	-1	< 13.81	-1	< 13.81	-1	< 13.81	9.2	8.1
J143511.53+360437.2	0.3876	-100.0	100.0	-50.9 ± 15.3	...	112.7 ± 21.6	...	14.70 ^{+0.27} _{-0.38}	-3	< 14.12	-1	< 14.12	-1	< 14.12	5.9	5.5
J143748.28-014710.7	0.2989	-90.0	55.0	< 12.89	-1	< 13.15	-1	< 13.15	-1	< 13.15	28.6	28.9
J143748.28-014710.7	0.6127	-90.0	60.0	-18.3 ± 2.9	-4.2 ± 7.0	112.8 ± 4.0	118.6 ± 9.9	13.90 ^{+0.03} _{-0.03}	0	13.83 ^{+0.07} _{-0.08}	0	13.83 ^{+0.07} _{-0.08}	0	13.83 ^{+0.07} _{-0.08}	22.0	22.1
J143748.28-014710.7	0.6812	-100.0	100.0	-4	< 13.41	-1	< 13.41	-1	< 13.41	...	20.4
J150030.64+551708.8	0.3473	-75.0	75.0	< 13.21	-1	< 13.59	-1	< 13.59	-1	< 13.59	13.2	12.0
J150030.64+551708.8	0.3480	-80.0	75.0	-5.8 ± 4.0	...	110.0 ± 5.7	...	14.04 ^{+0.04} _{-0.05}	0	< 13.64	-1	< 13.64	-1	< 13.64	13.0	12.9
J152424.58+095829.7	0.5185	-70.0	70.0	< 13.06	-1	...	-4	...	-4	...	18.4	...
J152424.58+095829.7	0.5718	-55.0	30.0	< 13.20	-1	< 13.36	-1	< 13.36	-1	< 13.36	11.1	13.7
J152424.58+095829.7	0.6754	-70.0	105.0	6.1 ± 3.2	11.1 ± 5.6	134.1 ± 4.5	133.2 ± 7.9	14.15 ^{+0.03} _{-0.03}	0	14.20 ^{+0.05} _{-0.06}	0	14.20 ^{+0.05} _{-0.06}	0	14.20 ^{+0.05} _{-0.06}	15.3	16.1

Table 2 continued

Table 2 (continued)

Target	z_{abs}	v_{min} (km s^{-1})	v_{max} (km s^{-1})	$\langle v \rangle$ (km s^{-1})	$\langle v \rangle$ (km s^{-1})	Δv_{90} (km s^{-1})	Δv_{90} (km s^{-1})	Δv_{90} (km s^{-1})	$\log N$ [cm^{-2}]	Detection	Flag	$\log N$ [cm^{-2}]	Detection	Flag	S/N	S/N
(1)	(2)	(3)	(4)	(5)	(6)	(7)	(8)	(9)	(10)	(11)	(12)	(13)	(14)	(15)	(16)	(17)
J152424.58+095829.7	0.7289	-30.0	50.0	3.3 ± 4.5	...	55.7 ± 6.3	...	$13.69^{+0.08}_{-0.10}$	0	...	-4	...	-4	10.2
J154121.48+281706.2	0.2825	-120.0	120.0	-9.1 ± 16.2	...	169.9 ± 22.9	...	$14.18^{+0.10}_{-0.13}$	0	< 13.89	-1	< 13.89	-1	6.8	8.4	8.4
J155048.29+400144.9	0.3126	-100.0	100.0	< 13.59	-1	< 13.92	-1	< 13.92	-1	8.4	7.8	7.8
J155048.29+400144.9	0.4273	-80.0	110.0	26.9 ± 4.7	15.3 ± 7.8	150.2 ± 6.6	156.6 ± 11.1	$14.37^{+0.04}_{-0.04}$	0	$14.37^{+0.06}_{-0.07}$	0	$14.37^{+0.06}_{-0.07}$	0	10.6	10.6	10.6
J155048.29+400144.9	0.4920	-90.0	90.0	...	-27.0 ± 4.5	...	113.8 ± 6.4	< 13.46	-1	$14.88^{+0.07}_{-0.08}$	-3	$14.88^{+0.07}_{-0.08}$	-3	11.1	10.8	10.8
J155048.29+400144.9	0.4926	-50.0	50.0	< 13.33	-1	< 13.61	-1	< 13.61	-1	11.3	10.4	10.4
J155232.54+570516.5	0.3660	-85.0	65.0	18.2 ± 5.9	20.4 ± 9.7	89.4 ± 8.4	95.1 ± 13.8	$14.12^{+0.05}_{-0.06}$	0	$14.21^{+0.08}_{-0.10}$	0	$14.21^{+0.08}_{-0.10}$	0	9.9	9.0	9.0
J155232.54+570516.5	0.3665	-50.0	55.0	-5.3 ± 2.5	-6.1 ± 5.6	76.5 ± 3.6	76.0 ± 7.9	$14.25^{+0.04}_{-0.05}$	0	$14.19^{+0.08}_{-0.10}$	0	$14.19^{+0.08}_{-0.10}$	0	9.7	8.5	8.5
J155304.92+354828.6	0.2179	-50.0	40.0	-7.5 ± 3.3	-8.9 ± 7.4	57.3 ± 4.6	71.3 ± 10.5	$13.98^{+0.06}_{-0.07}$	0	$13.94^{+0.12}_{-0.16}$	0	$13.94^{+0.12}_{-0.16}$	0	8.7	10.4	10.4
J155304.92+354828.6	0.4755	-75.0	75.0	< 13.54	-1	< 13.86	-1	< 13.86	-1	9.1	9.2	9.2
J155504.39+362848.0	0.5760	-75.0	75.0	< 13.81	-1	< 14.13	-1	< 14.13	-1	4.4	5.0	5.0
J161916.54+334238.4	0.2694	-70.0	70.0	19.4 ± 3.5	6.4 ± 10.9	73.0 ± 5.0	75.3 ± 15.4	$14.46^{+0.06}_{-0.07}$	-3	$13.86^{+0.11}_{-0.16}$	0	$13.86^{+0.11}_{-0.16}$	0	9.7	12.2	12.2
J161916.54+334238.4	0.4423	-75.0	100.0	< 13.13	-1	< 13.47	-1	< 13.47	-1	19.1	18.6	18.6
J161916.54+334238.4	0.4708	-50.0	100.0	31.2 ± 0.8	42.7 ± 2.4	101.9 ± 1.2	110.6 ± 3.3	$14.93^{+0.02}_{-0.02}$	0	$15.38^{+0.04}_{-0.04}$	-3	$15.38^{+0.04}_{-0.04}$	-3	19.0	17.4	17.4
J163201.12+373749.9	0.2740	-60.0	25.0	-11.8 ± 1.1	0.1 ± 2.3	95.4 ± 1.6	54.4 ± 3.2	$14.16^{+0.01}_{-0.01}$	-3	$13.94^{+0.04}_{-0.04}$	0	$13.94^{+0.04}_{-0.04}$	0	18.1	26.5	26.5
J163201.12+373749.9	0.4177	-60.0	65.0	8.6 ± 2.5	-2.5 ± 7.3	94.1 ± 3.5	83.0 ± 10.4	$13.72^{+0.03}_{-0.03}$	0	$13.69^{+0.09}_{-0.11}$	0	$13.69^{+0.09}_{-0.11}$	0	27.1	24.8	24.8
J215647.46+224249.8	0.5928	-30.0	40.0	3.8 ± 4.7	3.3 ± 14.1	67.3 ± 6.6	75.5 ± 20.0	$13.89^{+0.11}_{-0.14}$	0	$15.00^{+0.24}_{-0.57}$	-3	$15.00^{+0.24}_{-0.57}$	-3	6.7	6.3	6.3
J215647.46+224249.8	0.6200	-50.0	50.0	< 13.60	-1	< 13.87	-1	< 13.87	-1	7.0	6.8	6.8
J215647.46+224249.8	0.6210	-50.0	43.0	< 13.57	-1	< 13.86	-1	< 13.86	-1	7.1	6.7	6.7
J215647.46+224249.8	0.6214	-27.0	50.0	< 13.53	-1	< 13.83	-1	< 13.83	-1	7.0	6.6	6.6
J225357.75+160853.1	0.3206	-40.0	40.0	-0.2 ± 4.7	-4.4 ± 6.5	59.4 ± 6.7	59.1 ± 9.1	$13.90^{+0.09}_{-0.12}$	0	$14.09^{+0.12}_{-0.16}$	0	$14.09^{+0.12}_{-0.16}$	0	7.7	7.9	7.9
J225738.20+134045.4	0.4989	-40.0	80.0	-17.3 ± 5.5	24.8 ± 6.9	137.6 ± 7.7	92.4 ± 9.7	$14.42^{+0.07}_{-0.08}$	-3	$14.29^{+0.09}_{-0.11}$	0	$14.29^{+0.09}_{-0.11}$	0	7.2	8.0	8.0
J234500.43-005936.0	0.5481	-75.0	100.0	-9.5 ± 18.0	...	128.6 ± 25.4	...	$14.65^{+0.25}_{-0.68}$	-3	< 14.24	-1	< 14.24	-1	4.8	4.8	4.8

Table 2 continued

Table 2 (*continued*)

Target	z_{abs}	v_{min} (km s^{-1})	v_{max} (km s^{-1})	$\langle v \rangle$ (km s^{-1})	Δv_{90} (km s^{-1})	Δv_{90} (km s^{-1})	Δv_{90} (km s^{-1})	$\log N$ [cm^{-2}]	Detection	Flag	$\log N$ [cm^{-2}]	Detection	Flag	Detection	S/N	S/N
(1)	(2)	(3)	(4)	(5)	(6)	(7)	(8)	(9)	(10)	(11)	(12)	(13)	(14)	(15)	(16)	(17)

NOTE—(1) J-Name of the background quasar; (2) Redshift of the absorber; (3) Start velocity of the integration range; (4) End velocity of the integration range; (5) Average velocity centroid of O VI $\lambda 1031$; (6) Average velocity centroid of O VI $\lambda 1037$; (7) Velocity width of absorption for O VI $\lambda 1031$; (8) Velocity width of absorption for O VI $\lambda 1037$; (9) Measured column density of the $\lambda 1031$ transition; (10) Detection Flag for $\lambda 1031$ transition—0—detection, -1—upper limit, -2—saturation, -3—contaminated, -4—not covered by the spectrum; (11) Measured column density of the $\lambda 1037$ transition; (12) Detection Flag for $\lambda 1037$ transition; (13) S/N of the spectrum per pixel for O VI $\lambda 1031$; (14) S/N of the spectrum per pixel for O VI $\lambda 1037$.

Table 3. Adopted properties of the O VI absorbers in the robust sample

Target	z_{abs}	v_{min} (km s^{-1})	v_{max} (km s^{-1})	$\langle v \rangle$ (km s^{-1})	Δv_{90} (km s^{-1})	$\log N$ [cm^{-2}]	Detection Flag
(1)	(2)	(3)	(4)	(5)	(6)	(7)	(8)
J000559.23+160948.9	0.3058	-100.0	40.0	-52.0 ± 8.8	46.9 ± 12.5	$13.38^{+0.08}_{-0.10}$	0
J000559.23+160948.9	0.3479	-50.0	20.0	-19.2 ± 0.9	56.7 ± 1.2	$13.99^{+0.02}_{-0.02}$	0
J000559.23+160948.9	0.3662	-50.0	50.0	-0.3 ± 1.9	82.5 ± 2.6	$14.02^{+0.03}_{-0.03}$	0
J004222.29-103743.8	0.3161	-60.0	70.0	-4.4 ± 7.8	72.7 ± 11.1	$13.97^{+0.09}_{-0.12}$	0
J004705.89+031954.9	0.3139	-50.0	50.0	< 13.39	-1
J004705.89+031954.9	0.3143	-50.0	100.0	< 13.48	-1
J011013.14-021952.8	0.2272	-110.0	100.0	-22.5 ± 2.2	123.0 ± 3.2	$14.48^{+0.02}_{-0.02}$	0
J011013.14-021952.8	0.5365	-20.0	40.0	4.1 ± 4.2	34.8 ± 6.0	$13.59^{+0.11}_{-0.15}$	0
J011016.25-021851.0	0.3991	-100.0	80.0	-6.5 ± 3.3	116.1 ± 4.6	$14.36^{+0.03}_{-0.03}$	0
J011016.25-021851.0	0.5354	-50.0	40.0	< 13.44	-1
J011935.69-282131.4	0.3483	-60.0	10.0	< 13.09	-1
J011935.69-282131.4	0.3487	-100.0	40.0	-34.4 ± 3.3	89.8 ± 4.7	$14.07^{+0.04}_{-0.04}$	0
J012236.76-284321.3	0.3650	-45.0	80.0	18.5 ± 2.2	76.4 ± 3.1	$13.97^{+0.03}_{-0.03}$	0
J015513.20-450611.9	0.2260	-100.0	120.0	7.8 ± 1.9	108.1 ± 2.7	$14.18^{+0.02}_{-0.02}$	0
J020157.16-113233.1	0.3226	-50.0	50.0	< 12.89	-1
J020157.16-113233.1	0.3231	-40.0	25.0	-3.4 ± 3.1	52.6 ± 4.4	$13.27^{+0.07}_{-0.09}$	0
J020157.16-113233.1	0.3234	-55.0	70.0	< 13.29	-1
J020157.16-113233.1	0.3245	-45.0	85.0	16.2 ± 1.3	99.9 ± 1.8	$14.11^{+0.02}_{-0.02}$	0
J023507.38-040205.6	0.3225	-40.0	40.0	-1.6 ± 2.9	66.1 ± 4.1	$13.58^{+0.05}_{-0.06}$	0
J024337.66-303048.0	0.3037	-70.0	70.0	< 13.24	-1
J024649.86-300741.3	0.3123	-60.0	100.0	25.6 ± 6.1	106.2 ± 8.6	$14.13^{+0.06}_{-0.07}$	0
J024649.86-300741.3	0.3359	-50.0	70.0	< 13.44	-1
J035128.56-142908.0	0.3285	-70.0	100.0	-0.9 ± 11.6	92.3 ± 16.3	$13.57^{+0.10}_{-0.12}$	0
J035128.56-142908.0	0.3569	-160.0	120.0	-23.2 ± 4.0	159.5 ± 5.7	$14.69^{+0.03}_{-0.03}$	0
J035128.56-142908.0	0.3572	0.0	70.0	< 13.34	-1
J035128.56-142908.0	0.4398	-100.0	100.0	-7.1 ± 6.0	85.7 ± 8.5	$13.96^{+0.05}_{-0.05}$	0
J040148.98-054056.5	0.2195	-50.0	140.0	40.8 ± 2.8	134.0 ± 4.0	$14.53^{+0.03}_{-0.03}$	0
J040148.98-054056.5	0.3238	-70.0	70.0	< 13.45	-1
J040748.42-121136.3	0.1672	-125.0	95.0	-33.8 ± 0.4	149.2 ± 0.5	$14.63^{+0.00}_{-0.00}$	0
J040748.42-121136.3	0.3607	-30.0	30.0	0.3 ± 2.5	45.1 ± 3.5	$12.81^{+0.07}_{-0.08}$	0
J044011.90-524818.0	0.3279	-80.0	80.0	< 13.18	-1
J044011.90-524818.0	0.6150	-120.0	135.0	6.9 ± 2.3	176.7 ± 3.2	$14.86^{+0.02}_{-0.02}$	0
J044011.90-524818.0	0.6157	-20.0	80.0	16.0 ± 5.3	72.8 ± 7.5	$13.85^{+0.07}_{-0.09}$	0

Table 3 continued

Table 3 (continued)

Target	z_{abs}	v_{min}	v_{max}	$\langle v \rangle$	Δv_{90}	$\log N$	Detection
		(km s^{-1})	(km s^{-1})	(km s^{-1})	(km s^{-1})	[cm^{-2}]	Flag
(1)	(2)	(3)	(4)	(5)	(6)	(7)	(8)
J055224.49-640210.7	0.3451	-25.0	25.0	< 12.67	-1
J055224.49-640210.7	0.4461	-65.0	65.0	-1.9 ± 3.2	81.8 ± 4.5	$13.66^{+0.04}_{-0.04}$	0
J063546.49-751616.8	0.4175	-50.0	95.0	18.2 ± 1.3	100.9 ± 1.9	$14.16^{+0.02}_{-0.02}$	0
J063546.49-751616.8	0.4528	-20.0	100.0	41.0 ± 4.1	80.9 ± 5.8	$13.63^{+0.05}_{-0.06}$	0
J063546.49-751616.8	0.4685	-40.0	80.0	10.1 ± 3.3	81.5 ± 4.6	$13.69^{+0.04}_{-0.04}$	0
J071950.89+742757.0	0.3777	-40.0	70.0	9.1 ± 3.4	69.4 ± 4.8	$13.77^{+0.05}_{-0.05}$	0
J075112.30+291938.3	0.4318	-60.0	80.0	13.2 ± 3.8	89.7 ± 5.4	$13.52^{+0.04}_{-0.05}$	0
J075112.30+291938.3	0.4945	-30.0	50.0	4.4 ± 6.2	57.2 ± 8.7	$13.02^{+0.10}_{-0.14}$	0
J080908.13+461925.6	0.6191	-90.0	90.0	1.5 ± 3.2	92.5 ± 4.5	$14.74^{+0.04}_{-0.04}$	0
J091440.38+282330.6	0.2442	-90.0	70.0	-18.3 ± 4.0	107.1 ± 5.7	$14.42^{+0.05}_{-0.05}$	0
J092554.44+453544.5	0.3096	-50.0	50.0	< 13.12	-1
J094331.61+053131.4	0.2290	-50.0	50.0	< 13.50	-1
J100102.64+594414.2	0.4156	-60.0	25.0	< 13.05	-1
J100102.64+594414.2	0.4160	-80.0	125.0	17.8 ± 2.0	122.7 ± 2.8	$14.46^{+0.02}_{-0.02}$	0
J100535.25+013445.5	0.4185	-60.0	60.0	-7.9 ± 7.7	90.7 ± 10.8	$13.39^{+0.09}_{-0.11}$	0
J100535.25+013445.5	0.4197	-40.0	40.0	< 12.94	-1
J100902.06+071343.8	0.3372	-65.0	40.0	< 13.52	-1
J101622.60+470643.3	0.4322	-62.0	52.0	< 13.51	-1
J104117.16+061016.9	0.6544	-20.0	40.0	< 13.26	-1
J104117.16+061016.9	0.6551	-50.0	30.0	< 13.38	-1
J104117.16+061016.9	0.6554	-36.0	50.0	< 13.39	-1
J105945.24+144143.0	0.4658	-60.0	50.0	< 13.21	-1
J105945.24+144143.0	0.5765	-60.0	80.0	21.6 ± 7.7	95.1 ± 10.9	$13.91^{+0.08}_{-0.10}$	0
J105956.14+121151.1	0.3324	-60.0	60.0	< 13.43	-1
J110539.79+342534.3	0.2388	-60.0	65.0	0.4 ± 1.7	77.2 ± 2.4	$14.59^{+0.03}_{-0.03}$	0
J111132.20+554725.9	0.6175	-40.0	75.0	< 13.24	-1
J111132.20+554725.9	0.6827	-60.0	20.0	< 13.22	-1
J111507.65+023757.5	0.3692	-40.0	30.0	-7.8 ± 3.9	57.2 ± 5.5	$13.78^{+0.09}_{-0.11}$	0
J111754.23+263416.6	0.3520	-40.0	50.0	6.4 ± 6.8	77.7 ± 9.7	$13.68^{+0.11}_{-0.14}$	0
J111754.23+263416.6	0.3523	-30.0	60.0	< 13.37	-1
J111908.59+211918.0	0.1385	-95.0	95.0	7.8 ± 2.6	95.4 ± 3.7	$13.80^{+0.02}_{-0.02}$	0
J112553.78+591021.6	0.6784	-65.0	65.0	< 13.40	-1
J113457.71+255527.8	0.4320	-60.0	30.0	-17.0 ± 4.9	67.5 ± 6.9	$13.77^{+0.08}_{-0.10}$	0
J113457.71+255527.8	0.4323	-40.0	70.0	< 13.34	-1
J113910.70-135044.0	0.3195	-75.0	40.0	-19.4 ± 1.8	84.3 ± 2.5	$14.02^{+0.03}_{-0.03}$	0

Table 3 continued

Table 3 (continued)

Target	z_{abs}	v_{min}	v_{max}	$\langle v \rangle$	Δv_{90}	$\log N$	Detection
		(km s^{-1})	(km s^{-1})	(km s^{-1})	(km s^{-1})	[cm^{-2}]	Flag
(1)	(2)	(3)	(4)	(5)	(6)	(7)	(8)
J113956.98+654749.1	0.3257	-75.0	80.0	6.5 ± 1.4	84.1 ± 2.0	$13.97^{+0.01}_{-0.01}$	0
J113956.98+654749.1	0.5279	-60.0	10.0	-19.6 ± 5.9	49.0 ± 8.4	$13.08^{+0.11}_{-0.16}$	0
J115120.46+543733.0	0.2525	-110.0	140.0	7.6 ± 1.8	126.0 ± 2.5	$14.34^{+0.01}_{-0.01}$	0
J115120.46+543733.0	0.6886	-60.0	60.0	< 13.19	-1
J121430.55+082508.1	0.3247	-40.0	60.0	< 13.36	-1
J121430.55+082508.1	0.3838	-100.0	100.0	< 13.59	-1
J121920.93+063838.5	0.2823	-25.0	90.0	15.4 ± 3.3	79.2 ± 4.7	$13.63^{+0.04}_{-0.04}$	0
J122317.79+092306.9	0.3795	-50.0	40.0	< 13.32	-1
J122454.44+212246.3	0.3784	-80.0	80.0	1.5 ± 2.6	88.5 ± 3.6	$14.05^{+0.03}_{-0.03}$	0
J122454.44+212246.3	0.4208	-40.0	20.0	< 12.98	-1
J122454.44+212246.3	0.4214	-60.0	60.0	-10.4 ± 4.5	67.3 ± 6.4	$13.75^{+0.05}_{-0.06}$	0
J122512.93+121835.7	0.3250	-100.0	100.0	< 13.53	-1
J123304.05-003134.1	0.3188	-160.0	100.0	-36.1 ± 2.3	159.3 ± 3.2	$14.69^{+0.02}_{-0.02}$	0
J123335.07+475800.4	0.2849	-60.0	60.0	0.3 ± 5.3	54.3 ± 7.5	$13.93^{+0.08}_{-0.09}$	0
J124154.02+572107.3	0.2179	-100.0	40.0	4.7 ± 1.8	66.1 ± 2.6	$14.51^{+0.03}_{-0.03}$	0
J124511.26+335610.1	0.5876	-50.0	50.0	< 13.42	-1
J125846.65+242739.1	0.2262	-100.0	100.0	< 13.54	-1
J130429.02+311308.2	0.3099	-11.0	100.0	39.1 ± 2.1	86.4 ± 2.9	$14.30^{+0.03}_{-0.03}$	0
J130451.40+245445.9	0.2763	-75.0	75.0	< 13.43	-1
J133045.15+281321.5	0.2755	-80.0	90.0	7.1 ± 3.7	104.0 ± 5.3	$14.29^{+0.04}_{-0.04}$	0
J134100.78+412314.0	0.3488	-85.0	95.0	-2.3 ± 1.3	96.6 ± 1.8	$14.52^{+0.02}_{-0.02}$	0
J134100.78+412314.0	0.6208	-100.0	50.0	-0.5 ± 3.9	105.6 ± 5.6	$14.35^{+0.04}_{-0.05}$	0
J134100.78+412314.0	0.6214	-80.0	130.0	$14.91^{+0.02a}_{-0.02}$	0
J134100.78+412314.0	0.6861	-60.0	150.0	53.4 ± 3.5	101.1 ± 4.9	$14.80^{+0.07b}_{-0.07}$	0
J135726.26+043541.3	0.6102	-40.0	75.0	6.5 ± 2.4	79.9 ± 3.4	$14.41^{+0.04}_{-0.05}$	0
J140732.25+550725.4	0.2433	-75.0	75.0	< 13.36	-1
J140732.25+550725.4	0.2469	-50.0	50.0	< 13.29	-1
J140923.90+261820.9	0.5749	-50.0	100.0	< 13.05	-1
J140923.90+261820.9	0.5996	-50.0	40.0	-8.7 ± 1.2	80.2 ± 1.6	$13.99^{+0.02}_{-0.02}$	0
J140923.90+261820.9	0.6827	-85.0	85.0	2.0 ± 2.1	93.8 ± 3.0	$14.08^{+0.02}_{-0.02}$	0
J141038.39+230447.1	0.3498	-20.0	40.0	11.2 ± 2.6	45.2 ± 3.6	$13.83^{+0.07}_{-0.09}$	0
J141038.39+230447.1	0.3510	-50.0	55.0	< 13.40	-1
J141038.39+230447.1	0.5351	-20.0	75.0	23.8 ± 4.5	76.7 ± 6.4	$13.73^{+0.07}_{-0.09}$	0
J141910.20+420746.9	0.4256	-70.0	10.0	-27.9 ± 5.3	60.4 ± 7.5	$13.73^{+0.10}_{-0.13}$	0
J142859.03+322506.8	0.3823	-20.0	80.0	23.9 ± 4.9	56.7 ± 6.9	$13.79^{+0.08}_{-0.09}$	0

Table 3 continued

Table 3 (continued)

Target	z_{abs}	v_{min}	v_{max}	$\langle v \rangle$	Δv_{90}	$\log N$	Detection
		(km s^{-1})	(km s^{-1})	(km s^{-1})	(km s^{-1})	[cm^{-2}]	Flag
(1)	(2)	(3)	(4)	(5)	(6)	(7)	(8)
J143511.53+360437.2	0.3730	-60.0	60.0	< 13.46	-1
J143748.28-014710.7	0.2989	-90.0	55.0	< 12.89	-1
J143748.28-014710.7	0.6127	-90.0	60.0	-16.3 ± 2.6	113.6 ± 3.7	$13.89_{-0.03}^{+0.03}$	0
J143748.28-014710.7	0.6812	-100.0	100.0	< 13.41	-1
J150030.64+551708.8	0.3473	-75.0	75.0	< 13.21	-1
J150030.64+551708.8	0.3480	-80.0	75.0	-5.8 ± 4.0	110.0 ± 5.7	$14.04_{-0.05}^{+0.04}$	0
J152424.58+095829.7	0.5185	-70.0	70.0	< 13.06	-1
J152424.58+095829.7	0.5718	-55.0	30.0	< 13.20	-1
J152424.58+095829.7	0.6754	-70.0	105.0	7.4 ± 2.8	133.9 ± 3.9	$14.16_{-0.03}^{+0.03}$	0
J152424.58+095829.7	0.7289	-30.0	50.0	3.3 ± 4.5	55.7 ± 6.3	$13.69_{-0.10}^{+0.08}$	0
J155048.29+400144.9	0.3126	-100.0	100.0	< 13.59	-1
J155048.29+400144.9	0.4273	-80.0	110.0	23.8 ± 4.0	151.9 ± 5.7	$14.37_{-0.04}^{+0.04}$	0
J155048.29+400144.9	0.4920	-90.0	90.0	< 13.46	-1
J155048.29+400144.9	0.4926	-50.0	50.0	< 13.33	-1
J155232.54+570516.5	0.3660	-85.0	65.0	18.8 ± 5.1	90.9 ± 7.2	$14.14_{-0.05}^{+0.05}$	0
J155232.54+570516.5	0.3665	-50.0	55.0	-5.4 ± 2.3	76.4 ± 3.3	$14.24_{-0.04}^{+0.04}$	0
J155304.92+354828.6	0.2179	-50.0	40.0	-7.8 ± 3.0	59.6 ± 4.2	$13.98_{-0.06}^{+0.06}$	0
J155304.92+354828.6	0.4755	-75.0	75.0	< 13.54	-1
J161916.54+334238.4	0.2694	-70.0	70.0	6.4 ± 10.9	75.3 ± 15.4	$13.86_{-0.16}^{+0.11}$	0
J161916.54+334238.4	0.4423	-75.0	100.0	< 13.13	-1
J163201.12+373749.9	0.2740	-60.0	25.0	0.1 ± 2.3	54.4 ± 3.2	$13.94_{-0.04}^{+0.04}$	0
J163201.12+373749.9	0.4177	-60.0	65.0	7.5 ± 2.3	93.0 ± 3.3	$13.72_{-0.03}^{+0.03}$	0
J225738.20+134045.4	0.4989	-40.0	80.0	24.8 ± 6.9	92.4 ± 9.7	$14.29_{-0.11}^{+0.09}$	0

NOTE—^a For the $z = 0.6214$ absorber towards J134100.78+412314.0, we found that both the O VI transitions were affected by contamination to different extents in the velocity range of integration. For this system, we have summed the column densities measured over different velocity ranges for both transitions, avoiding regions of contamination. We have also not measured $\langle v \rangle$ and Δv_{90} for this system because both transitions are affected by contamination in different velocity ranges. ^b For the $z = 0.6861$ absorber towards J134100.78+412314.0, we found evidence for saturation in the O VI $\lambda 1031$ line, which we corrected for (see text for more detail).

For H I, C II, and C III, we adopt the column densities, kinematics, and integration ranges from CCC I. For multiple transitions of a given species detected at more than 2σ and uncontaminated (e.g., C II, H I), CCC I used a variance-weighted mean of the measurements when no saturation was present. Saturation was assessed using atoms or ions with multiple transitions (see Section 4.2 in CCC I for more detail). For single transitions (such as C III), saturation was evaluated by determining at which peak optical depth there is evidence for satura-

tion in species with multiple transitions; if saturation is present, the column density is reported as a lower limit with a 0.15 dex correction applied (see explanation in §4.2 of CCC I). For the H I transitions, only the weaker transitions were considered (i.e., Ly α , Ly β , and typically Ly γ were excluded). The H I column densities were derived from the mean of the values calculated using two to three methods for the SLFSs and pLLSs, including the AOD method, Voigt profile fitting, and a curve-of-growth analysis (see CCC I for more details).

We remind the reader that the velocity ranges over which the absorption lines were integrated in CCC I were selected using the weakest HI absorption transitions so that the absorbers consist as much as possible of a single HI absorbing complex at the COS resolution and in these transitions. However, in a few cases for the pLLSs ($\lesssim 10\%$ of the present sample) and LLSs, stronger HI transitions may show an additional, weaker component(s). Such an example is the absorber toward J035128.56–142908.0 at $z = 0.439804$ where HI $\lambda\lambda 917, 918$ show little evidence of an additional component (see CCC I), but a blended component is evident in the stronger HI transitions shown in the figures of the Appendix (which is located at $\approx -50 \text{ km s}^{-1}$ relative to the stronger absorption component). In that case, the additional component adds ≈ 0.1 dex to the N_{HI} value of the pLLS.

While we adopt the integration ranges from CCC I for the low ions and HI, we cannot apply the same integration ranges for O VI. The O VI profiles can be more extended than HI or shifted in velocity relative to the HI. A re-analysis of the velocity integration ranges for O VI is therefore required (see also Footnote 10 in CCC I). Our methodology to select $[v_{\text{min}}, v_{\text{max}}]$ for integrating the O VI $\lambda\lambda 1031, 1037$ profiles is as follows: 1) if the stronger transitions of HI indicate no blending with a weaker HI absorber, we consider the entire velocity range over which the O VI absorption is observed; 2) if there is some evidence for an additional blend in the HI transitions with a weaker HI absorber (or absorbers), v_{min} and/or v_{max} are set to the values determined from the HI. This approach minimizes the inclusions of other HI absorbers in the O VI absorption. In both cases, v_{min} and v_{max} may be somewhat adjusted if there is some evidence of contamination in one of the O VI transitions. In Fig. 1, we show as an example the $N_a(v)$ profiles of O VI, C II, C III, and HI of a blended system with two components that are treated each as an individual absorber.

As part of revisiting the integration range for O VI, we also conducted a visual inspection of all the continua near the two O VI transitions. This reexamination was needed, as the CCC I work focused on lower ionization gas and did not emphasize O VI absorption in their analysis. The continuum regions used for the continuum fit with low-order Legendre polynomials were automatically selected following the method described in CCC I. In $\sim 20\%$ of the cases, we determined that the continua could be improved and adjusted the continua by manually selecting the continuum regions to be fit with the Legendre polynomials. In 92% of these manually adjusted cases, the resulting column densi-

ties were similar (within $\lesssim 0.05$ dex) to those derived in CCC I using the same velocity intervals for the integration. For 8% of these cases (3 absorbers), the new continua led to a larger difference of about 0.10–0.15 dex (the largest value being for an absorber with unresolved saturation that was not assessed as such in CCC I; see below). These continuum readjustments also resulted in improved agreement (all within 1σ , see below) between the column density measurements derived from the two O VI transitions.

When deriving the kinematics and column densities of the O VI $\lambda\lambda 1031, 1037$ doublet, we encounter various scenarios, which we detail below. The simplest case is when O VI $\lambda 1031$ is not detected at the 3σ level. In this case, we adopt the 2σ column density upper limit derived from the equivalent width uncertainty, assuming the line lies on the linear portion of the curve of growth, and adopting the same integration range as that of HI.

In the case where both transitions of the O VI doublet are available, we determine if the absorption is saturated by comparing their integrated column densities and $N_a(v)$ profiles. Saturation can cause the integrated column density derived from the weaker transition to be larger than that derived from the stronger transition. However, contamination can also produce a similar effect. To distinguish between these two possibilities, we visually inspected the profiles to determine if any discrepancy occurs at or near the peak optical depth, where saturation effects are most prominent. We found consistency between the two O VI transitions at the $\approx 1\sigma$ confidence level and column density profiles (see an example in Fig. 1), implying no saturation, even for O VI absorbers with $\log N(\text{O VI}) \gtrsim 14.5$ with the exception of one absorber at redshift $z = 0.6861$ toward J134100.78+412314.0. For this system, the weaker transition exhibits a marginally higher column density (by 0.05 dex) compared to the stronger transition, although still within 1σ . The $N_a(v)$ profile comparison reveals that this discrepancy is localized in the absorption core, strongly suggesting saturation, which we corrected for using the method outlined in Savage & Sembach (1991).

To identify contamination, we employ a similar procedure, but in this case, either transition may yield a larger integrated column density. The appendix figures illustrate several instances of partial or complete contamination. Some examples of unambiguous contamination include absorbers at $z = 0.356924$ toward J035128.56–142908.0 and at $z = 0.619130$ toward J080908.13+461925.6, where O VI $\lambda 1031$ is affected. A more nuanced case is the absorber at $z = 0.378447$ toward J122454.44+212246.3, where O VI $\lambda 1037$ shows contamination. In this instance, the discrepancy is ev-

ident at peak optical depth and persists at low optical depths in the negative velocity wing, where the $N_a(v)$ profiles should match (as they do at positive velocities), leading to its classification as contaminated. For the $z = 0.6214$ absorber towards J134100.78+412314.0, both O VI transitions exhibit contamination at different velocities. To address this, we have aggregated the column densities measured over distinct velocity ranges for both transitions, excluding contaminated regions.

Among the 73 detected absorbers in our robust sample (see Section 4.1), six cases have only the O VI $\lambda 1031$ transition. For these instances, we classify a detection as clean when it is neither affected by nor is an interloper after visually inspecting the absorption velocity profile relative to those observed in H I and other ions. For these single-transition systems, we found no evidence of saturation in the O VI absorption, as the peak optical depth consistently remains $\lesssim 1$.

We summarize in Table 2 the results ($\langle v \rangle$, Δv_{90} , $\log N$) for each transition of the O VI doublet. All listed uncertainties are 1σ values while upper limits are given at the 2σ level. The $N_a(v)$ and normalized flux profiles for all the systems with O VI coverage from the CCC are presented as supplementary materials in the appendix. In Table 3, we tabulate the adopted O VI measurements for the robust sample. All the listed uncertainties correspond to 1σ values. Upper limits are again given at the 2σ level. When both transitions of the doublet are detected at $> 3\sigma$ with no evidence of saturation or contamination (see above), the adopted column densities and kinematics are a weighted mean between the two transitions. The uncertainty on the logarithmic of the column density is obtained following the prescription in §2.8 of Barlow (2003) to account for the possible asymmetric uncertainties in the measurements. In the one case of saturation, we adopt the column density from the weak transition after correcting for saturation following the procedure above; in that case, the kinematics are adopted from the weak transition. If one of the transitions is contaminated, we adopt the results from the uncontaminated transition.

4. RESULTS

Below, we present the empirical properties of O VI absorption associated with H I-selected absorbers whose metallicities have been systematically determined. As previously discussed, we adopt the metallicities of the cool photoionized gas from CCC III. Following the definitions in CCC II and CCC III, we classify absorption systems as low-metallicity (LM) when $[X/H] \leq -1.4$ and high-metallicity (HM) when $[X/H] > -1.4$ (see Section 2).

4.1. Frequency of O VI

The frequency or detection rate is a sample-dependent heuristic that represents the fraction of detected O VI absorption systems within a given H I absorber sample. We compute these rates assuming a binomial distribution, following the method of Cameron (2011). This approach assesses the likelihood function for detection rate values, given the number of detections relative to the total number in a chosen subsample. Cameron demonstrates that the normalized likelihood function used for estimating Bayesian confidence intervals on a binomial distribution with a uniform prior follows a β distribution. For a detailed discussion of this method, which is particularly suitable for robust determination of detection rates, we refer the reader to Cameron (2011) (see also Howk et al. 2017). We report the median of the distribution along with asymmetric uncertainties corresponding to the 16th and 84th percentiles.

Our robust sample includes 100 SLFSs and 26 pLLSs (see Table 1). We remind that our robust sample has $S/N \geq 8$ per resolution element yielding sensitivity to absorbers with $\log N(\text{O VI}) \geq 13.6$ at the 2σ level (see Section 2); the interquartile range (IQR) of S/N is [10, 19] with a median of 12. We summarize the detection rates as a function of H I-selected and metallicity-selected subsamples in Table 4. In the 43 SLFSs with O VI non-detections, the 2σ upper limits on the O VI column density range from $\log N(\text{O VI}) < 13.6$ to $\log N(\text{O VI}) < 12.9$; in the 9 pLLSs with O VI non-detections, the 2σ upper limits on the O VI column density range from $\log N(\text{O VI}) < 13.6$ to $\log N(\text{O VI}) < 12.7$. The detection rates are therefore determined by treating measured values below the survey sensitivity of $\log N(\text{O VI}) < 13.6$ as non-detections.

The detection rates of O VI in SLFSs and pLLSs are found to be $48 \pm 5\%$ and $61 \pm 9\%$, respectively. Although O VI detection rates overlap between SLFSs and pLLSs, there is a suggestion of a somewhat lower frequency of O VI with $\log N(\text{O VI}) \geq 13.6$ in SLFSs than in pLLSs (but see below). For comparison, Fox et al. (2013), who studied the properties of the intermediate ions and high ions in 23 pLLSs, reported a O VI detection rate of $83^{+8}_{-9}\%$ in their survey of pLLSs at the 3σ level, calculated accounting for the detection sensitivity of their survey, consistent with our value for pLLSs within 1.75σ .

We find that the HM sample has a significantly higher ($> 4\sigma$) O VI detection rate of $63 \pm 5\%$ compared to $28^{+7}_{-6}\%$ for the LM sample. However, this difference is driven by the low frequency of O VI in LM SLFSs since the detection rates in the HM and LM pLLSs and HM SLFSs are similar $\sim 60\%$ (see Table 4). While there are

Table 4. Detections rates of O VI for different subsamples

Sample	Size	Detection Rate (%)
SLFSs + pLLSs	126	51 ± 4
SLFSs	100	48 ± 5
pLLSs	26	61 ± 9
LM	44	28^{+7}_{-6}
HM	82	63 ± 5
SLFSs-LM	36	21^{+7}_{-6}
SLFSs-HM	64	64 ± 6
pLLSs-LM	8	61^{+15}_{-16}
pLLSs-HM	18	60 ± 11

NOTE—LM refers to the low-metallicity subsample, and HM refers to the metal-enriched subsample. The median value and the uncertainties of the distribution corresponding to the 16th and 84th percentiles are given. The detection rates are calculated at the survey sensitivity of $\log N(\text{O VI}) \geq 13.6$.

only 8 systems in the LM pLLS sample, there is the same balance of HM and LM absorbers in the pLLSs and SLFSs, with $\sim 2/3$ HM and $\sim 1/3$ LM. Therefore the high frequency of O VI with LM pLLSs compared to LM SLFSs is unlikely to arise owing to small statistical numbers and the smaller frequency of O VI with $\log N(\text{O VI}) \geq 13.6$ in SLFSs than pLLSs is driven by the LM SLFS sample.

4.2. $\log N(\text{O VI})$ - $\log N(\text{H I})$ Relationship

In Fig. 2, we plot the relationship between $\log N(\text{O VI})$ and $\log N(\text{H I})$, and color code it by the metallicity of the lower-ionization gas. Visually we do not see an apparent correlation between the parameters of $\log N(\text{O VI})$ - $\log N(\text{H I})$ for either the LM or the HM sample. Danforth & Shull (2005), using an O VI-selected sample, found a very mild relationship between $N(\text{O VI})$ and $N(\text{H I})$, and fit the relation with a $N(\text{H I})^{0.1}$ power law over the H I column density of $13 \lesssim \log N(\text{H I}) \lesssim 16$. We test for a correlation between the O VI and H I column densities by performing the ATS test. This test performs linear regression for bivariate data accounting for the upper limits, and quantifies the null-hypothesis probability. We test the null hypothesis of no correlation between $\log N(\text{O VI})$ and $\log N(\text{H I})$. For the robust, HM, and LM samples, we obtain p -values $\gg 0.05$, i.e., the null hypothesis cannot be rejected. In contrast, CCC I

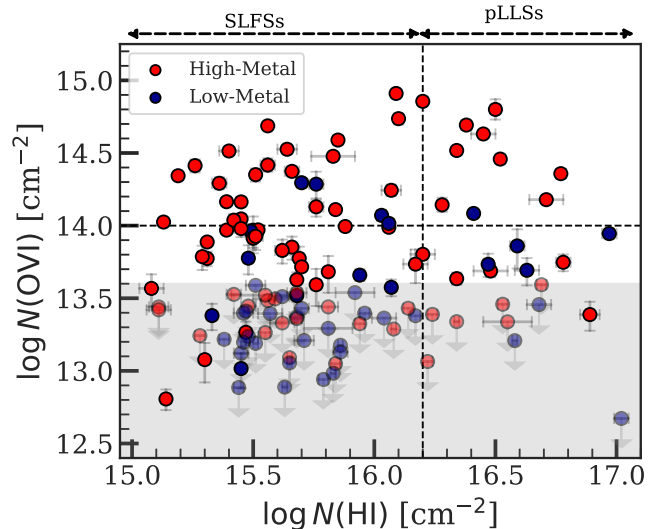


Figure 2. O VI column density as a function of the H I column density. The vertical line divides the sample into SLFSs and pLLSs. The horizontal line separates the sample based on $\log N(\text{O VI}) = 14$. The data points are color-coded by the metallicity of lower ionization gas. The HM sample is shown in red and the LM sample is shown in blue. Upper limits on O VI column density measurements are shown as grey downward pointing arrows. The light-shaded region highlights the sensitivity limit of our survey of $\log N(\text{O VI}) \geq 13.6$.

found evidence for a significant correlation between the column densities of the singly and doubly ionized species of carbon with H I in the $15 \leq \log N(\text{H I}) \leq 17$ range (see their Figure 11). The strong association between low- and intermediate ions, and H I indicates that these ions likely exist in the same gas phase, and indeed single-phase photoionization models reproduce quite well the column densities of these ions (CCC II; CCC III). Conversely, the absence of substantial correlation between $\log N(\text{O VI})$ and $\log N(\text{H I})$ suggests that O VI is likely located in a separate phase from the lower-ionization gas.

4.3. O VI Kinematics

4.3.1. Average Central Velocities

We consider the statistic of kinematic velocity centroid offset, $v_X - v_{\text{H I}}$, between the absorption component in a metal ion, X , from H I.⁵ It provides information on how absorbing ions are distributed in veloc-

⁵ For saturation-affected features, we determine the velocity centroid using a treatment similar to that for unsaturated profiles. The primary effect of saturation is to decrease the true weight of the line core velocities relative to the wings in the centroid calculation. In our analysis, C III is the ion most affected by saturation effects: 37/94 C III, 1/31 C II, and 1/73 O VI absorbers in our robust sample exhibit saturation. As discussed in

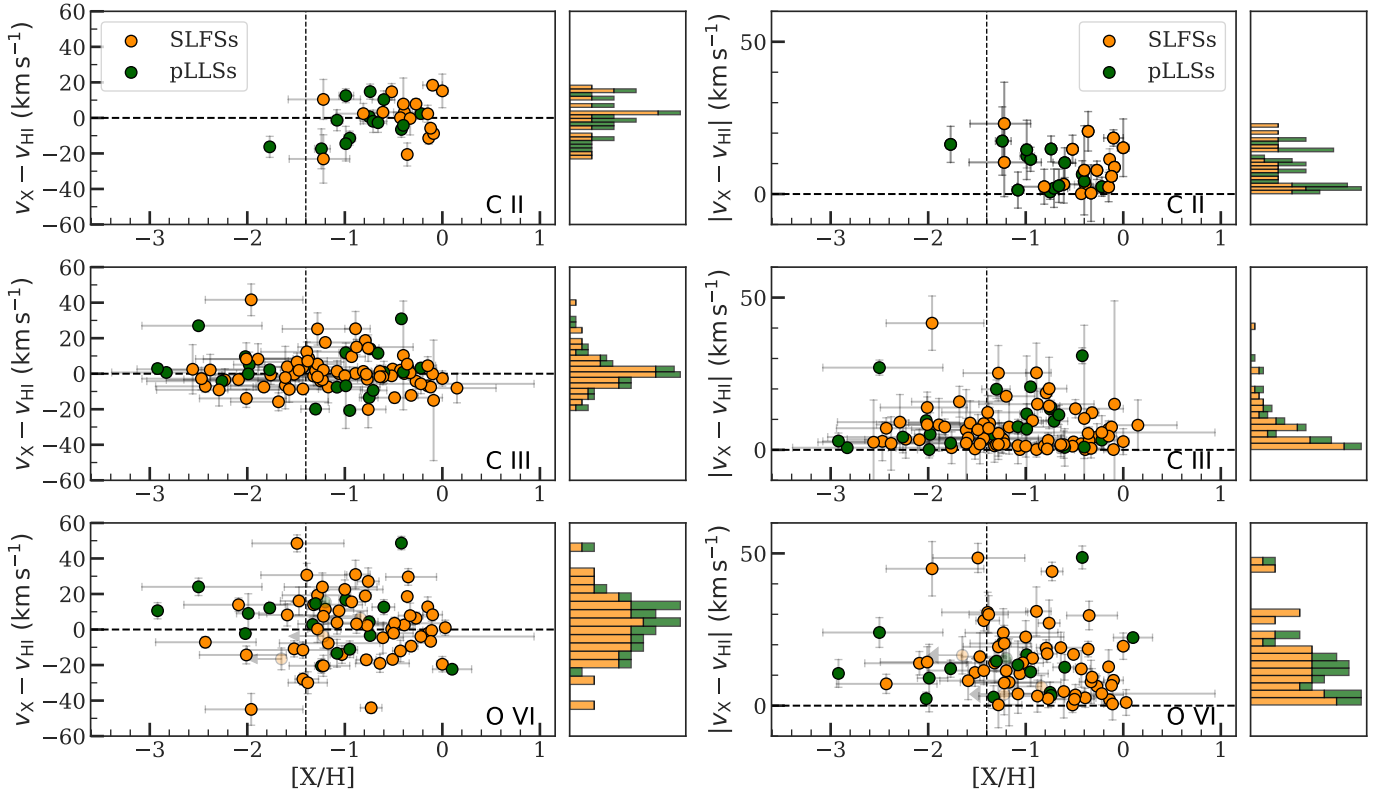


Figure 3. Comparison of (*left*) velocity centroid offset and (*right*) absolute velocity centroid offset, with metallicity for C II, C III, and O VI. The vertical line marks the separation between low metallicity and HM absorbers. The horizontal line marks the mean of the sample. SLFSs are colored in orange, while pLLSs are colored in green. The stacked histograms to the right are presented to highlight the dispersion in the velocity centroid offsets

ity space within each absorption system.⁶ Such velocity offsets can indicate a multiphase structure of the absorption system (Fox et al. 2013). S14 noted that velocity centroid offsets between O VI and Ly α absorption components, $|v_{\text{O VI}} - v_{\text{HI}}| > 10 \text{ km s}^{-1}$, often indicate that these ions reside in separate phases based on a detailed comparison of the H I and O VI velocity profiles observed in the highest-S/N *HST*/COS G130M/G160M spectra.

Section 1, we employ a Monte Carlo sampling approach to account for measurement errors. For saturated absorption features, we modify this approach to mitigate the influence of less robustly constrained velocity centroids. Instead of drawing from a normal distribution, we sample from a uniform distribution ranging between the minimum and maximum values corresponding to one standard deviation below and above the mean velocity centroid value. This uniform distribution sampling for saturated absorbers aims to capture a broader range of possible centroid values and reduce the impact of less reliable saturated core velocities on our statistical analysis.

⁶ CCC I found that the absolute COS wavelength calibration to be accurate within one COS resolution element ($\approx 15 \text{ km s}^{-1}$; see also Holland et al. 2012) using the Lyman series transitions. Consequently, any velocity shifts larger than $\gtrsim 15 \text{ km s}^{-1}$ likely represent real velocity differences rather than data artefacts.

In the left panels of Fig. 3, we plot the velocity centroid offset, $v_X - v_{\text{HI}}$, of low ion (C II), intermediate ion (C III), and high ion (O VI) species, as a function of metallicity. To the right of each scatter plot, we present a histogram showing the distribution of velocity centroid offsets for the corresponding ion. The C II histogram displays a relatively flat distribution in the range of $[-20, 20] \text{ km s}^{-1}$, though the sample size is comparatively small. For C III, the histogram exhibits a symmetric distribution centered near zero km s^{-1} and fewer data points extending to large positive or negative offsets. In contrast, the O VI histogram reveals a much broader distribution compared to C II and C III. While its peak is close to $\approx 0 \text{ km s}^{-1}$, the distribution shows considerable dispersion, with many data points well beyond $\pm 20 \text{ km s}^{-1}$ —far exceeding offsets that could be attributed to COS wavelength calibration.

In Fig. 3 (right), we show the absolute velocity centroid offsets, $|v_X - v_{\text{HI}}|$, and their distributions for C II, C III, and O VI. The IQR, mean, and 1σ dispersion values for $|v_X - v_{\text{HI}}|$ are tabulated in Table 5. Fox et al. (2013) in their sample of pLLSs find the absolute veloc-

Table 5. Summary statistics of $|v_X - v_{\text{HI}}|$ values for different ions

Ion (X)	Sample Size	IQR (km s^{-1})	$\mu \pm \sigma_\mu$ (km s^{-1})	σ (km s^{-1})
C II	31	3–15	9 ± 1	7
C III	94	2–10	7 ± 1	8
O VI	73	6–19	14 ± 1	11
C II–SLFSs	17	3–15	9 ± 2	7
C II–pLLSs	14	2–14	8 ± 2	6
C III–SLFSs	72	2–9	7 ± 1	7
C III–pLLSs	22	3–13	9 ± 1	9
O VI–SLFSs	56	6–19	14 ± 1	11
O VI–pLLSs	17	9–17	14 ± 1	11
C III–LM	32	2–8	7 ± 1	8
C III–HM	62	2–12	8 ± 1	7
O VI–LM	16	10–18	17 ± 1	13
O VI–HM	57	4–19	13 ± 1	11

NOTE—We do not estimate the summary statistics for C II–LM since there is only one data point.

ity centroid offsets to be $6 \pm 1 \text{ km s}^{-1}$, $10 \pm 2 \text{ km s}^{-1}$ and $14 \pm 4 \text{ km s}^{-1}$ for C II, C III and O VI ions, respectively, consistent with our findings for pLLSs in our sample. We note that there is a large dispersion in the velocity centroid offsets for the various ions as tabulated in the last column of Table 5.

To investigate any differences in the $|v_X - v_{\text{HI}}|$ distributions of the LM and HM groupings of C III and O VI, we perform a two-sample Anderson-Darling (AD) test for the null hypothesis that the two samples are identical. AD test is a non-parametric test and can be more powerful than the KS test for smaller sample sizes ($\lesssim 25$) (Epps & Singleton 1986). We obtain p -values $\gg 0.05$ for both C III and O VI, implying that the null hypothesis cannot be rejected. We do not perform the AD test for C II because of only one data point in LM grouping for C II.

We also perform the AD test to compare the $|v_X - v_{\text{HI}}|$ distributions of low, intermediate, and high ions irrespective of the metallicity. We find a statistically significant difference in the $|v_X - v_{\text{HI}}|$ distributions of C III compared with O VI with p -value of 0.001 ± 0.001 . But, C II does not show a statistically significant difference compared with O VI (p -value = 0.15 ± 0.18). C II also

does not a statistically significant difference in the velocity centroid offsets compared with C III (p -value $\gg 0.05$). We note that the results for C II could be affected by the small sample sizes and, hence, may not be statistically meaningful. These results suggest that the intermediate ion of C III and O VI do not always arise in a single phase and could imply a multiphase medium. We further compare the $|v_X - v_{\text{HI}}|$ distributions of SLFSs and pLLSs for each of the ions of C II, C III and O VI, but do not find evidence for a statistically significant difference in their distributions with p -values $\gg 0.05$.

4.3.2. Velocity Widths

Another indicator of kinematic differences is the velocity width, Δv_{90} (see Section 3). We measure it for four species: H I, C II, C III, and O VI. In Fig. 4, we plot the velocity width, Δv_{90} , as a function of metallicity. The IQR, mean, and 1σ dispersion values for Δv_{90} are tabulated in Table 6. To handle the measurements associated with saturated C III absorbers, the velocity width was randomly drawn from a uniform distribution spanning the range from 30 km s^{-1} to the upper limit value when generating 1000 replicated datasets. We chose the lower bound of 30 km s^{-1} because it is about the smallest velocity width observed for unsaturated C III absorption in our sample. The O VI sample exhibits a noticeably broader velocity width when compared to the low and intermediate metal ions.

We observe that the mean value of Δv_{90} for the O VI HM sample is greater than that of O VI LM sample. We perform the MWU test, a non-parametric test, to compare the O VI Δv_{90} distribution associated with HM lower-ionization gas and the O VI Δv_{90} distribution associated with LM lower-ionization gas. This statistical test is used to determine if there is a significant difference between the average values of two distributions. We find that O VI Δv_{90} distribution associated with HM population is statistically greater than the O VI Δv_{90} distribution associated with LM population (p -value = 0.03 ± 0.02). We do not find evidence for a statistically significant difference in the Δv_{90} distributions of LM and HM gas for H I and C III with p -values $\gg 0.05$.

The primary conclusion from our kinematic analysis is that low and intermediate ions exhibit relatively smaller centroid offsets and line widths compared to the O VI ion. From these results, we draw two main inferences: i) the lower-ionization gas and O VI do not always trace the same plasma, and ii) there are distinct differences in the kinematic properties of O VI associated with low-metallicity (LM) and high-metallicity (HM) lower-ionization gas.

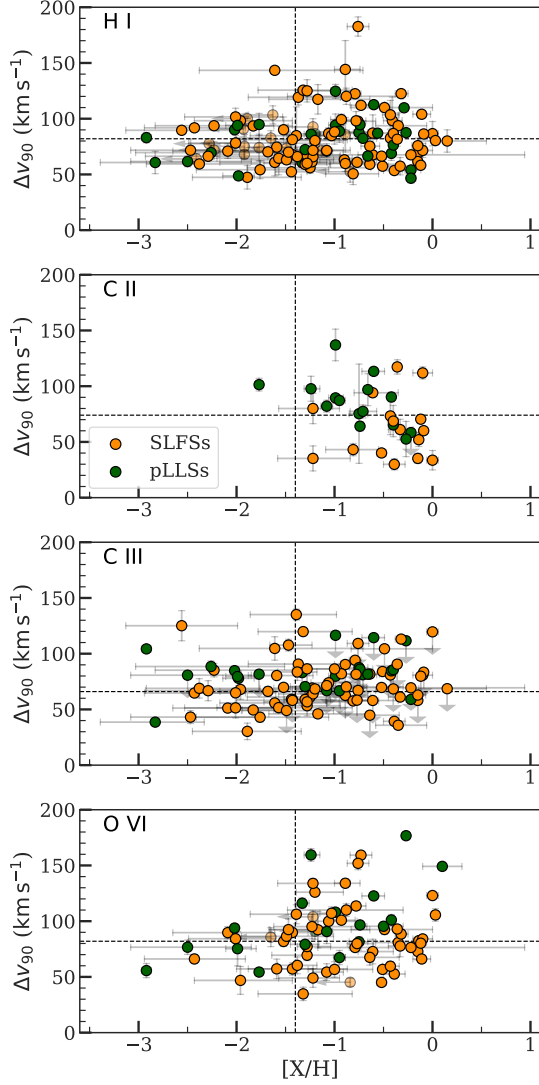


Figure 4. Comparison of velocity width, Δv_{90} , with metallicity for H I, C II, C III, and O VI. The vertical line marks the separation between LM and HM absorbers. The horizontal line marks the mean value of velocity width. SLFSs are colored in orange, while pLLSs are colored in green. Saturated absorption is seen mainly in C III and is presented as upper limits.

4.4. O VI Column Densities

We measure O VI absorption at a significance level of 3σ or above in 73 of the 126 associated H I components. Our upper limits for non-detected absorption are reported at the 2σ level⁷. The IQR of the $\log N(\text{O VI})$

⁷ To determine if a line is detected or not detected, we compare the measured equivalent width within the velocity range of integration, EW , to the total uncertainty on the equivalent width within the velocity range of integration, EW_{err} , (accounting for both the statistical uncertainty and continuum uncertainty). If the condition $EW \geq 3EW_{\text{err}}$ is met, we consider the line to be

Table 6. Summary statistics of Δv_{90} values for different ions

Atom/Ion	Sample	IQR	$\mu \pm \sigma_\mu$	σ
	Size	(km s^{-1})	(km s^{-1})	(km s^{-1})
H I	126	66–93	82 ± 1	22
C II	31	56–92	74 ± 2	27
C III	94	61–89	67 ± 1	21
O VI	73	67–101	89 ± 1	32
H I–LM	44	66–90	78 ± 1	18
H I–HM	82	66–95	84 ± 1	24
C III–LM	32	53–83	66 ± 1	22
C III–HM	62	65–91	67 ± 2	26
O VI–LM	16	57–87	75 ± 2	16
O VI–HM	57	73–107	92 ± 1	31

NOTE—We do not estimate the summary statistics for C II–LM since there is only one data point. The IQR for C III is determined by treating the upper limits on Δv_{90} as measured values.

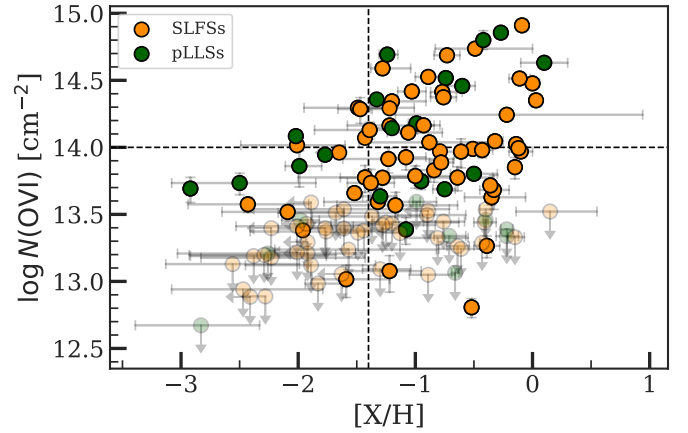


Figure 5. The O VI column density as a function of metallicity for our sample. O VI detections are shown as dark-filled circles, the non-detections (upper limits) are shown as filled circles with attached downward-pointing arrows and shaded in a lighter tone. The vertical line divides the sample into LM and HM subsamples. The horizontal line at $\log N(\text{O VI}) = 14$ divides the sample based on the O VI absorption strength. The data points are color-coded to differentiate SLFSs (orange) and pLLSs (green).

detected at the 3σ level. If not, we report the linear column density measurement corresponding to $2EW_{\text{err}}$ as the upper limit value.

in our robust sample is 12.81–14.00, accounting for the upper limits. The mean of the O VI column density distribution and the standard error on the mean are $\log \langle N(\text{O VI}) \rangle = 13.98 \pm 0.01$, estimated using the KM estimator accounting for the upper limits.⁸ The geometric mean and the standard error on the geometric mean are $\langle \log N(\text{O VI}) \rangle = 13.52 \pm 0.02$. Considering just the detections, we obtain mean and geometric mean values of $\log \langle N(\text{O VI}) \rangle = 14.21 \pm 0.01$ and $\langle \log N(\text{O VI}) \rangle = 14.01 \pm 0.01$.

Motivated by the inference from the O VI kinematics that the O VI and lower ionization gas likely reside in different gas phases, we next investigate the trend between the O VI column density and metallicity. We would expect a correlation if the properties of the different phases are linked. In Fig. 5, we plot the column density of O VI as a function of the cool gas metallicity derived in CCC III. On average, the HM systems ($[X/H] > -1.4$) show stronger O VI absorption when compared to the LM systems. We find that when $\log N(\text{O VI}) \geq 14$, only $16^{+7}_{-5}\%$ of the systems are associated with LM gas. But strikingly, $84^{+5}_{-7}\%$ of the systems with $\log N(\text{O VI}) \geq 14$ are associated with HM gas. The IQR for the HM and LM subsamples spans between 13.08–14.24 dex and 12.89–13.68 dex, respectively. The geometric means of O VI column density for HM and LM subsamples are $\langle \log N(\text{O VI}) \rangle = 13.73 \pm 0.02$ and 13.22 ± 0.05 , respectively. The means of O VI column density for HM and LM subsamples are $\log \langle N(\text{O VI}) \rangle = 14.11 \pm 0.01$ and 13.46 ± 0.02 , respectively.

We observe a positive correlation between the O VI column density and metallicity of the cool gas. We perform the ATS test to investigate the null hypothesis of no correlation between these parameters, and find a p -value = $(0.6 \pm 0.9) \times 10^{-3}$, rejecting the null hypothesis. This suggests that the O VI column density and the metallicity of lower-ionization gas are correlated. The correlation between the column density of O VI and the metallicity of the cool photoionized gas is remarkable, given that the O VI and low-ionization gas were found to show statistically significant differences in kinematics and reside in different gas phases.

Fox et al. (2013) found similarly a trend in which metal-rich pLLSs showed higher O VI columns than metal-poor pLLSs. Consistent with their finding, we determine that the mean $\log N(\text{O VI})$ for HM pLLSs is higher than that of LM pLLSs with mean values

⁸ Hereafter, we use the notation of $\log \langle N(\text{O VI}) \rangle$ and $\langle \log N(\text{O VI}) \rangle$ to imply the mean of the O VI column density and the error on the mean, and the geometric mean of the O VI column density and the error on the geometric mean, respectively.

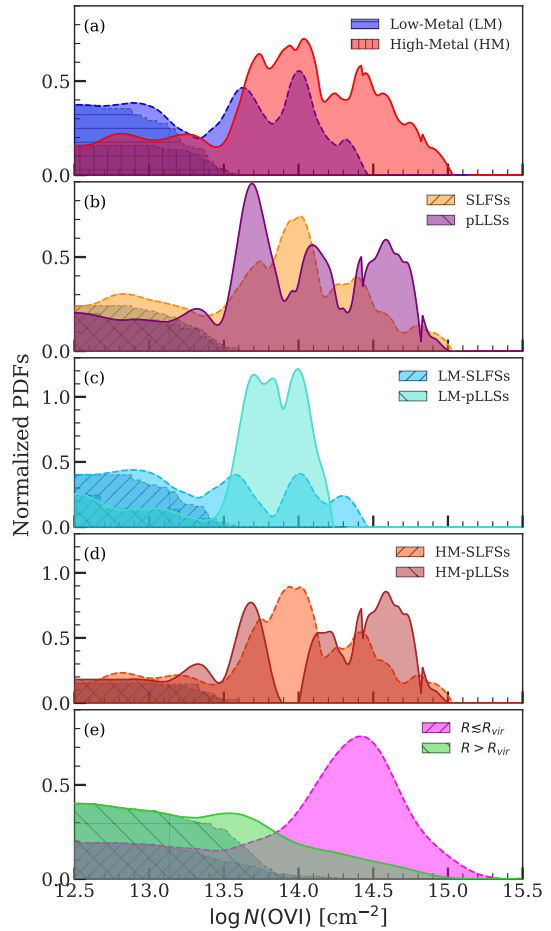


Figure 6. Normalized PDFs of O VI column density for the (a) LM subsample and the HM subsample; (b) for the SLFSs and pLLSs sub-samples; (c) for the LM-SLFSs and LM-pLLSs sub-samples; (d) for the HM-SLFSs and HM-pLLSs sub-samples; and (e) for absorbers within $\lesssim R_{\text{vir}}$ (103 absorbers) and absorbers beyond $> R_{\text{vir}}$ (146 absorbers) taken from T22. The contribution from the lower limits is shown with hatchings.

of $\log \langle N(\text{O VI}) \rangle = 14.20 \pm 0.02$ and 13.67 ± 0.03 , respectively. The geometric mean for the HM pLLSs and LM pLLSs are $\langle \log N(\text{O VI}) \rangle = 13.87 \pm 0.03$ and 13.57 ± 0.03 , respectively. We find that the O VI frequency with $\log N(\text{O VI}) \geq 14$ in LM pLLSs is $18^{+14}_{-10}\%$ compared with $45 \pm 11\%$ in HM pLLSs.

So far, we have considered the discrete distributions of the O VI column density; in Fig. 6, we display the normalized PDFs of O VI column density for various sub-samples. The detections are modeled by approximating them as a Fechner distribution accounting for asymmetric uncertainties in the O VI column density measurements. The upper limits are modeled as uniform distributions spanning a $\log N(\text{O VI})$ range of 11.5 dex to the estimated upper limit value. Our choice of the lower

bound of $\log N(\text{O VI}) = 11.5$ is motivated by the lowest O VI column densities predicted by EAGLE cosmological simulations (Oppenheimer et al. 2016). Figure 2 in their paper shows that the predicted O VI column densities extend down to $\log N(\text{O VI}) \approx 11.5$ for halos with masses between $10^{11.1} M_{\odot} < M_{200} < 10^{13.2} M_{\odot}$, with less prevalence of lower column density O VI gas at higher halo masses.

In Fig. 6a, we show the $\log N(\text{O VI})$ distributions of LM and HM lower-ionization gas. The LM PDF has two main peaks at $\log N(\text{O VI}) \approx 13.6$ and 14.0, and an important tail at $\log N(\text{O VI}) < 13.2$ dex; the detection rate for this subsample is only $28 \pm 7\%$, which is driven by the SLFS sample. The PDF of the HM subsample shows two apparent peaks at $\log N(\text{O VI}) \approx 13.9$ and 14.4, and a relatively weaker tail extending to $\log N(\text{O VI}) \lesssim 13.5$. Visually, the $\log N(\text{O VI})$ distributions of the LM and HM absorbers are quite different. Statistically, we compare the $\log N(\text{O VI})$ distributions of the LM and HM groupings to test the null hypothesis that they belong to the same underlying parent population, while accounting for the upper limits using the log-rank test (implemented using *survdiff* package in R language). The log-rank test does not assume the normality of the distributions and is a non-parametric test. We find a statistically significant difference in the distributions of LM and HM subsamples ($p\text{-value} = (4 \pm 1) \times 10^{-4}$). This result implies that the column densities of O VI absorbers arising in LM and HM systems are significantly different. As a reminder, we also found statistically significant differences ($p\text{-value} = 0.03 \pm 0.02$) in O VI velocity widths between LM and HM subsamples in Section 4.3.

We compare the $\log N(\text{O VI})$ distributions for the SLFSs and pLLSs in our sample in Fig. 6b. We observe that the SLFSs show a main peak at $\log N(\text{O VI}) \approx 14.0$ with a broad distribution below and above this value and several smaller peaks. The pLLSs, on the other hand, show three peaks - a dominant one and two smaller peaks at $\log N(\text{O VI}) \approx 13.7$, 14.1, and 14.6, respectively. We again perform the log-rank test for the null hypothesis that SLFSs and pLLSs are probing the same parent population of O VI absorbers but cannot reject the null hypothesis ($p\text{-value} \gg 0.05$).

Berg et al. (2023) found that the HM pLLSs are typically associated with galaxies, whereas LM pLLSs trace more diverse locations, including the IGM at the periphery of galaxies. To explore the relationship of O VI linked with LM and HM lower-ionization gas with the environments, we divide our sample into four groups based on metallicity-selection and H I-selection - LM-SLFSs, LM-pLLSs, HM-SLFSs, and HM-pLLSs. Figs. 6c and 6d show these four groupings. The O VI column den-

sity distribution of LM-SLFSs shows two small peaks at $\log N(\text{O VI}) \approx 13.5$ and 14, and it is dominated by upper-limits extending to lower column densities. This subsample has a detection rate of only $21 \pm 6\%$ (see Table 4). The O VI column density distribution of LM-pLLSs shows a broad peak centered at $\log N(\text{O VI}) \approx 13.9$, with a weaker tail arising from the upper-limits extending to lower column densities. The O VI column density distribution of HM-SLFSs shows a peak centered at $\log N(\text{O VI}) \approx 13.9$, with contribution from O VI column densities in the range $\log N(\text{O VI}) \approx 13.9\text{--}14.7$, and a weaker tail arising from the upper-limits extending to lower column densities. The O VI column density distribution of HM-pLLSs shows two peaks centered at $\log N(\text{O VI}) \approx 13.8$ and 14.5, and a relatively smaller peak at $\log N(\text{O VI}) \approx 14.2$, and a weaker tail arising from the upper-limits extending to lower column densities. The LM-pLLSs, HM-SLFSs, and HM-pLLSs, all have similar detection rates of $\approx 60\%$. However, Figs. 6c and 6d show that LM-pLLSs have O VI column densities well under $\log N(\text{O VI}) \lesssim 14.2$, while the O VI column density PDF of HM-SLFSs and HM-pLLSs show significant contributions from $\log N(\text{O VI}) \geq 14.2$.

We finally compare the O VI column density distributions of the above four groupings to the O VI column density distribution of absorbers within the virial radius ($\lesssim R_{\text{vir}}$) of their associated galaxy and those beyond $> R_{\text{vir}}$ from T22. The O VI column density distributions of absorbers from T22 segregated by R_{vir} is shown in Fig. 6e. The O VI absorbers within $\lesssim R_{\text{vir}}$ have an IQR that spans 13.36–14.44 dex, and a higher mean O VI column density, $\log \langle N(\text{O VI}) \rangle = 14.27 \pm 0.05$ ($\langle \log N(\text{O VI}) \rangle = 13.96 \pm 0.06$) than that of the $> R_{\text{vir}}$ population for the which the IQR spans 13.10–13.47 dex and has a mean of $\log \langle N(\text{O VI}) \rangle = 13.67 \pm 0.07$ ($\langle \log N(\text{O VI}) \rangle = 13.41 \pm 0.07$). The O VI column density PDF of the absorbers at $R \lesssim R_{\text{vir}}$ from galaxies shows a strongly peaked mode at $\log N(\text{O VI}) \approx 14.4$, with a long tail extending to lower column densities. The O VI column density PDF of absorbers at $R > R_{\text{vir}}$ from galaxies does not show any particular peak and is dominated by non-detections. To gain further insights into the association between O VI gas and the environments it may be tracing, we perform the log-rank to compare the $\log N(\text{O VI})$ distributions associated with metallicity-selected and H I-selected groupings with $\log N(\text{O VI})$ distributions of O VI absorbers segregated based on R_{vir} . We tabulated the p -values from the log-rank test in Table 7. Based on the p -values, we find that the O VI associated with LM-SLFSs is significantly different from the O VI arising within the R_{vir} of associated galaxies ($p\text{-value} = (12 \pm 1) \times 10^{-5}$), but no

Table 7. p -values from log-rank tests comparing O VI column density distributions: metallicity-selected and H I-selected groups vs. absorbers within ($R \lesssim R_{\text{vir}}$) and beyond ($R > R_{\text{vir}}$) the virial radius of associated galaxies.

Environment	LM-SLFSs	HM-SLFSs	LM-pLLSs	HM-pLLSs
$R \lesssim R_{\text{vir}}$	$(12 \pm 1) \times 10^{-5}$	0.32 ± 0.04	0.47 ± 0.03	0.78 ± 0.02
$R > R_{\text{vir}}$	0.91 ± 0.03	$(2 \pm 1) \times 10^{-11}$	0.002 ± 0.001	$(3 \pm 1) \times 10^{-5}$

NOTE—For the log-rank test, if $p \geq 0.05$, then the null-hypothesis is retained and both samples have identical distributions; if $p < 0.05$, then the null-hypothesis is rejected and both samples have different distributions.

significant differences are seen between O VI associated with LM-pLLSs and HM lower ionization gas, and O VI arising within R_{vir} of associated galaxies. On the other hand, O VI associated with LM-pLLSs and HM lower ionization gas is found to be significantly different from the O VI arising beyond R_{vir} of associated galaxies, but no significant differences are seen between O VI associated with LM-SLFSs and O VI beyond R_{vir} of associated galaxies.

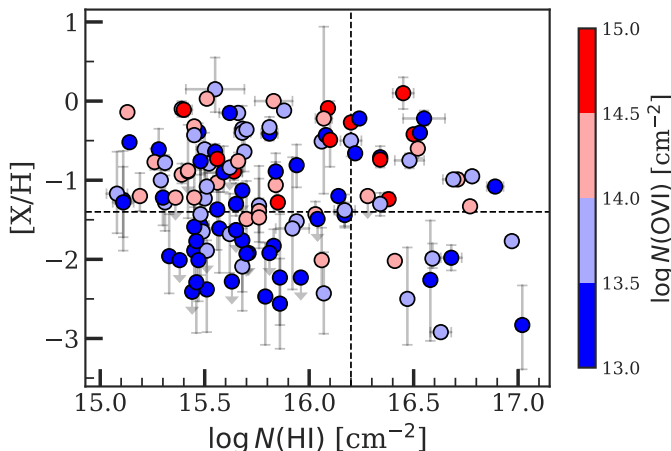


Figure 7. The metallicity of the cool gas as a function of H I column density for our sample. The data points are colored by their $\log N(\text{O VI})$. The horizontal line divides the sample into low-metal and high-metal subsamples. The vertical line divides the sample into SLFSs and pLLSs. About 80% of the absorbers with $\log N(\text{O VI}) < 13.6$ have no O VI detection.

5. DISCUSSION

5.1. Preamble

We have studied a sample of 126 H I-selected absorbers at $z \lesssim 1$ from the CCC survey with O VI $\lambda 1031$ and/or $\lambda 1037$ coverage in COS G130M/G160M spectra with $S/N \gtrsim 8$. The H I-selected absorbers span the H I col-

umn density range $15 \lesssim \log N(\text{H I}) \lesssim 17.2$. This H I column density range allows for these absorbers to be sensitive to both HM and LM gas at $z \lesssim 1$ (CCC I), so this sample has no bias with regard to the metallicity of the cool gas. There is also no bias with regard to the strength of the O VI absorption down to the sensitivity level of our survey, $\log N(\text{O VI}) \lesssim 13.6$. This contrasts remarkably from blind O VI surveys, which requires detection of O VI and probe mostly absorbers with $13 \lesssim \log N(\text{H I}) \lesssim 14.5$ (e.g., Danforth & Shull 2005; Tripp et al. 2008; Thom & Chen 2008a; S14). The H I-selection is also different from galaxy-centric surveys (e.g., Tumlinson et al. 2011; Werk et al. 2012; Stocke et al. 2013; Johnson et al. 2015; Keeney et al. 2017; Wilde et al. 2021; Tchernyshyov et al. 2023) because even though our survey probes overdensities of $\delta \approx 15$ –200 at $z \lesssim 1$ (using $N(\text{H I}) \propto (1 + \delta)^{1.5}$ where $\delta \equiv n_{\text{H}}/\bar{n}_{\text{H}}$ is the overdensity, see Schaye 2001), the H I-selection is agnostic in terms of the type and mass of the galaxies or the environments that these absorbers may probe (e.g., denser regions of the IGM instead of the CGM, intra-group gas, etc.). Therefore, the H I-selection provides a different perspective relative to blind O VI or galaxy-centric surveys. It is instructive therefore to compare our results to these surveys to understand the origin(s) of these absorbers.

From Section 4, we categorize the O VI absorbers into: (1) non-detections with $\log N(\text{O VI}) < 13.6$; (2) detections with $\log N(\text{O VI}) \lesssim 14$; and (3) detections with $\log N(\text{O VI}) \gtrsim 14$. To motivate this, Fig. 7 shows the $[X/H]$ – $N(\text{H I})$ distribution colored by $\log N(\text{O VI})$. A majority ($84^{+5}_{-7}\%$) of the absorbers with $\log N(\text{O VI}) \geq 14$ have high metallicities (100% for $\log N(\text{O VI}) \gtrsim 14.5$), while those with $\log N(\text{O VI}) < 14$ span all metallicities and H I columns. As Fig. 8 shows, category (3) absorbers tend to be also broader ($\Delta v_{90} \gtrsim 100 \text{ km s}^{-1}$) and/or have large O VI–H I velocity offsets ($|v_{\text{O VI}} - v_{\text{H I}}| \gtrsim 20$

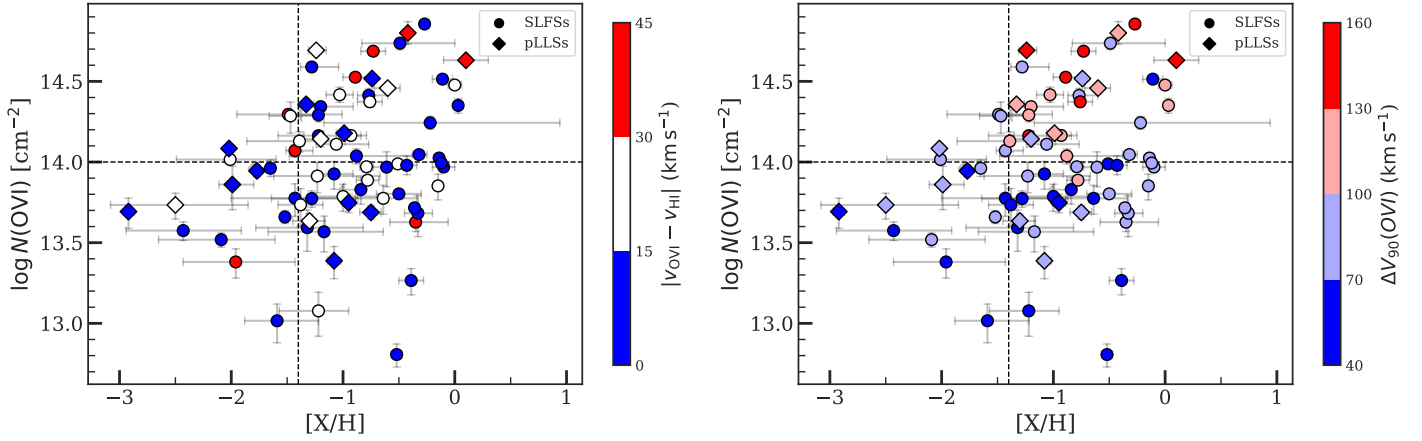


Figure 8. The O VI column density as a function of metallicity of the cool gas for absorbers with detected O VI in our sample colored by their kinematic properties. *Left:* colored by absolute velocity centroid offset, $|v_{\text{O VI}} - v_{\text{H I}}|$; *right:* velocity width, $\Delta v_{90}(\text{O VI})$.

km s^{-1}), possibly suggesting a galaxy feedback origin for these (see Section 5.5).

5.2. HI-Selected Absorbers with no O VI: Single-Phase Gas

While blind O VI surveys found very little evidence of O VI without associated H I (e.g., Thom & Chen 2008b; Savage et al. 2014; Keeney et al. 2017), $\sim 40\%$ of our H I-selected sample has no O VI detected down to $\log N(\text{O VI}) \lesssim 13.6$ (and even $\log N(\text{O VI}) \lesssim 13$ in several cases). Although previous blind surveys were sensitive to $\log N(\text{O VI}) \gtrsim 12.8\text{--}13.1$, most O VI systems are found with $\log N(\text{O VI}) \gtrsim 13.5$ (e.g., Tripp et al. 2008; S14). Hence, the lack of O VI absorption in our sample indicates a real deficit of highly ionized gas. Indeed, using spectra from CCC I, these absorbers show no other high ions (e.g., Ne VIII), and all remaining ions (excluding N and Fe ions, which were not typically included in these models) can be modeled by a single photoionized phase (CCC III).

The absence of O VI absorption in $\sim 40\%$ of absorbers therefore implies that these systems may probe a single-phase gas, in contrast with the frequent presence of multiphase gas in CGM absorbers (e.g., Zahedy et al. 2019; Sameer et al. 2021). The frequency of detected O VI with $\log N(\text{O VI}) \gtrsim 13.6$ is similar around 60% in HM SLFSs, LM and HM pLLSs (see Table 4), but it is substantially lower in LM SLFSs at $21 \pm 6\%$. This implies that pLLSs have, in general, a more complex gas-phase structure of the metallicities. Hence, LM SLFSs mostly probe single-phase gas, while HM SLFSs and pLLSs typically trace multiphase gas.⁹

⁹ Although they could also probe more complex regions where the O VI and lower ions may not be cospatial, this is unlikely to

In their survey of galaxies at $z \sim 0.2$, which is combined with the COS-Halos survey (Tumlinson et al. 2013), Johnson et al. (2015) found that the vast majority of the O VI non-detections were beyond the virial radius of galaxies, but these absorbers have H I column densities $\log N(\text{H I}) < 15$, i.e., much lower than those in our survey. A handful of O VI non-detections with $\log N(\text{O VI}) \lesssim 13.6$ are found within $\lesssim R_{\text{vir}}$ where $\log N(\text{H I}) \gtrsim 15$; the majority of these galaxies are early-type galaxies (see also T22 and Fig. 9). In the CGM² galaxy survey, the population of O VI non-detections is also predominantly found beyond R_{vir} (see Section 4.4 and Fig. 6c) (T22). This combined with the fact that the highest fraction of non-detections of O VI are found in LM absorbers, they may instead trace the overdense IGM, like some of the LM pLLSs (Berg et al. 2023). In addition, a fraction of these might be found in CGM ($\lesssim R_{\text{vir}}$) of dwarf galaxies with stellar masses of $\lesssim 10^8\text{--}10^9 M_{\odot}$ since 3/8 of the dwarfs in the sample of Johnson et al. (2017) have no O VI detection but have relatively strong H I absorption ($\log N(\text{H I}) \gtrsim 14.5$).

5.3. HI-Selected Absorbers with O VI Detections: Multiple-Phase Gas

About 20% of the LM SLFSs and 60% of the LM/HM pLLSs and HM SLFSs have associated O VI absorption (see Table 4). As shown by many independent works studying the detailed ionization processes at play, photoionization models can generally match the H I, low and intermediate ions, but rarely O VI in the same gas phase at $z \lesssim 1$ as the EUVB is typically not hard enough and the densities too high to produce coexisting O VI and low

be systematic owing to the close velocity proximity of the H I and O VI velocities that are separated by $\lesssim 40 \text{ km s}^{-1}$, see Fig. 3.

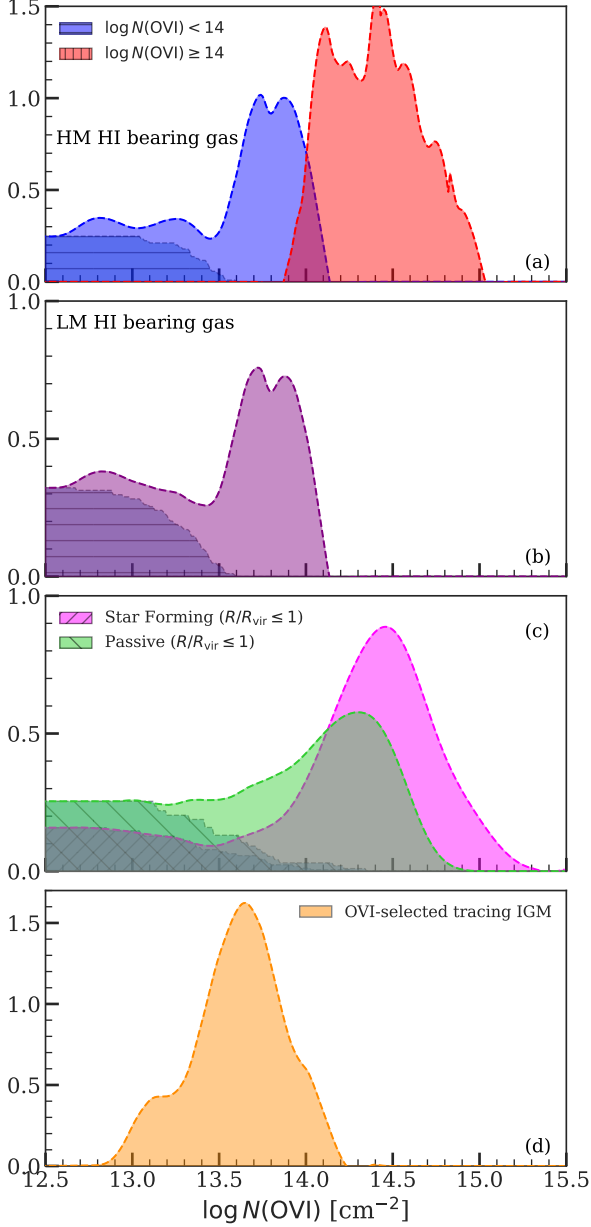


Figure 9. Normalized PDFs of O VI column density for the (a) HM lower-ionization gas comprising of strong O VI absorbers, $\log N(\text{O VI}) \geq 14$ (in red) and weaker O VI absorbers, $\log N(\text{O VI}) < 14$ (in blue); (b) LM lower-ionization gas excluding the one data point with $\log N(\text{O VI}) > 14$; (c) star-forming (67 in number) and passive (36 in number) galaxies from T22 within R_{vir} ; d) O VI-selected absorbers (22 in number) extending 200 to 600 kpc beyond the closest associated galaxies from the survey of S14. The contribution from the upper limits are shown with hatchings.

ions (e.g., Cooksey et al. 2008; Lehner et al. 2009, 2013; Kacprzak et al. 2012; Crighton et al. 2013; S14; Werk et al. 2016; Stocke et al. 2017; Rosenwasser et al. 2018; Zahedy et al. 2019; Cooper et al. 2021; Haislmaier et al.

2021; Sameer et al. 2021, 2024). Hence, detected O VI likely traces a separate hot, collisionally ionized phase, cooler collisionally ionized gas in non-equilibrium, or a very low-density photoionized phase distinct from the majority of H I gas at $z \lesssim 1$.

When we compare the velocity profiles between O VI, H I, C II, and C III, we find larger centroid offsets for O VI relative to H I compared to the lower ions (see Figs. 3 and 8), indicating O VI traces a distinct phase (e.g., S14). While the low/intermediate ions show consistent velocity width distributions between metallicity subsamples, O VI widths differ significantly, with HM absorbers being broader than LM absorbers (Fig. 4). This suggests intrinsic differences in the O VI-bearing gas related to metallicity, possibly owing to outflows driven or recycling material produced by high stellar activity within star-forming galaxies where higher metallicities and broader O VI absorbers are expected (e.g., Lehner et al. 2014; Lehner 2017; Werk et al. 2016; Qu et al. 2024).

5.4. H I-Selected Absorbers with $\log N(\text{O VI}) \lesssim 14$

Weak O VI absorption ($\log N(\text{O VI}) \lesssim 14$) in H I-selected absorbers shows little connection between the properties of O VI and the cool, lower ionization gas. This O VI can be found over the whole range of H I column densities and metallicities of our sample (Fig. 7). However, in contrast to their stronger analogs, the kinematics of the weak O VI in these absorbers are not as extreme; their velocity widths are typically $\Delta v_{90}(\text{O VI}) \lesssim 80 \text{ km s}^{-1}$ (Fig. 8).

In Figs. 9a, b, we show the O VI column density distributions for the HM and LM portions of our sample, respectively, splitting the O VI distributions for absorbers on either side of the $\log N(\text{O VI}) = 14$ threshold, which corresponds to the geometric mean of the sample with O VI detections (see §4.4). For comparison, we show the O VI column density distributions for absorbers projected within R_{vir} of star-forming and passive galaxies from T22 in Fig. 9c, while we show the distribution of O VI column densities for gas projected at large distances from the closest galaxies ($200 \leq R \leq 600 \text{ kpc}$) from S14 in Fig. 9d. Fig. 9 shows the weak O VI absorbers in the HM and LM groupings are not statistically different from one another ($p\text{-value} \gg 0.05$), and those are similar in many ways to that of the IGM sample at $R > R_{\text{vir}}$ (S14). A log-rank test comparing the weak LM and weak HM groupings with the IGM sample yields $p\text{-values} \gg 0.05$, in both cases, suggesting that these distributions are not significantly different from one another. Thus, the H I-selected absorbers with weak O VI may predominantly trace the IGM and extended CGM (beyond R_{vir}),

although a small population of weak absorbers is also seen in the tail of the galaxy-centered samples (and some of these may include dwarf galaxies, see Johnson et al. 2017; Qu et al. 2024).

5.5. HI-Selected Absorbers with $\log N(\text{O VI}) \gtrsim 14$

Similar to their weaker counterparts, HI-selected absorbers with strong O VI absorption ($\log N(\text{O VI}) \gtrsim 14$) show no correlation between their O VI and HI column densities. However, they exhibit a strong connection with the metallicity of the cool photoionized gas, as they are found nearly exclusively at $[\text{X}/\text{H}] > -1.4$. Out of 35 absorbers with $\log N(\text{O VI}) \gtrsim 14$, only 5 are found with $[\text{X}/\text{H}] \lesssim -1.4$. Using the same criterion to define the threshold between HM and LM gas at $z \sim 2.4\text{--}3.5$ places the split at $[\text{X}/\text{H}] = -2.4$ (Lehner et al. 2022b), above which strong O VI also predominates, implying that this relation is observed at any z . This is striking since the metallicities of the cool, lower ionization phase and the O VI-bearing gas can differ in multiphase absorbers (e.g., Savage et al. 2011; Muzahid et al. 2015; Cooper et al. 2021). The pronounced correlation suggests strong O VI and HM cool gas are likely produced by similar phenomena, such as galaxy feedback.

As shown in Figs. 6 and 9, strong O VI dominates in the CGM ($< R_{\text{vir}}$) of star-forming galaxies (Tumlinson et al. 2011; Johnson et al. 2015; T22), including those of some dwarf galaxies (Johnson et al. 2017; Qu et al. 2024). Tchernyshyov et al. (2023) find higher O VI covering fractions around star-forming galaxies across three galaxy mass ranges than about passive, quiescent galaxies (for $\log N(\text{O VI}) \gtrsim 14.3$). Werk et al. (2016) using the COS-halos sample show that very broad and strong O VI absorbers are defining characteristics of the CGM of star-forming L^* galaxies at $z \sim 0.2$. Berg et al. (2023) show HM gas occurs solely around star-forming, relatively massive galaxies. Given the behavior of $R < R_{\text{vir}}$ absorption, that the strong O VI absorbers in our sample are found exclusively in the HM population, and the corresponding large velocity breadths of much of our sample, there seems to be a robust link between strong O VI absorption and enriched gas within halos of star-forming galaxies.

As noted by Lehner et al. (2014) (see also Lehner 2017), the breadth ($\Delta v_{90}(\text{O VI}) \gtrsim 100 \text{ km s}^{-1}$) and strength ($\log N(\text{O VI}) \gtrsim 14.3$) of the O VI absorption in strong HI absorbers at high redshifts ($z \sim 2.4\text{--}3.5$) are strikingly similar to those observed in starburst galaxies at low redshift (e.g., Grimes et al. 2009; Muzahid et al. 2015; Tripp et al. 2008; Rosenwasser et al. 2018). Strong and broad O VI absorbers could, therefore, be a signature of large-scale feedback (outflowing or recycling) in

these high redshift galaxies. This could also be the case for the strong low-redshift O VI absorbers in view of their connection to the massive star-forming galaxies, especially for the 50% of the strong O VI absorbers that have a large breadth with $\Delta v_{90} \gtrsim 100 \text{ km s}^{-1}$ (see Fig. 8b). Recently, Qu et al. (2024) show that the O VI absorption is stronger and broader in star-forming galaxies than passive galaxies within R_{vir} at $z \sim 0.4\text{--}0.7$. These could arise in large-scale radiatively cooling gas behind a supersonic wind produced by galaxy starburst-driven winds (e.g., Heckman et al. 2002; Werk et al. 2016). Alternatively, some of these O VI absorbers could also be signatures of the hot halo corona themselves (e.g., Werk et al. 2016; Sameer et al. 2024), radiative cooling of galactic fountain gas (e.g., Sembach et al. 2001; Wakker et al. 2005; Lehner et al. 2022a; Marasco et al. 2022), or possibly active galactic nucleus (AGN) feedback (e.g., Oppenheimer et al. 2016; Suresh et al. 2016). Future observations of the galaxies in some of these fields should help better discern the origins of the strong O VI associated with these HI-selected absorbers.

6. SUMMARY

We studied the kinematics and absorption properties of O VI gas and their relationship with lower ionization gas in a HI-selected survey by analyzing the O VI absorption in a sample of 126 low- z absorption systems ($0.14 < z < 0.73$) observed in *HST*/COS G130M and/or G160M spectra with S/N $\gtrsim 8$ per resolution element and complete to $\log N(\text{O VI}) \gtrsim 13.6$ at the 2σ level. The main results are as follows:

1. The sample comprises 100 SLFSs and 26 pLLSs with O VI detection rates at a sensitivity level of $\log N(\text{O VI}) \gtrsim 13.6$ of about 50% and 60%, respectively. This difference is largely driven by the low-metal (LM; $[\text{X}/\text{H}] \leq -1.4$) SLFSs since their O VI detection rate is 20% compared to 60% for the high-metal (HM; $[\text{X}/\text{H}] > -1.4$) SLFSs and HM or LM pLLSs.
2. An empirical characterization of the profile kinematics shows that $\langle |v_{\text{C II}} - v_{\text{HI}}| \rangle = 9 \pm 7 \text{ km s}^{-1}$ and $\langle |v_{\text{C III}} - v_{\text{HI}}| \rangle = 7 \pm 8 \text{ km s}^{-1}$ compared to $\langle |v_{\text{O VI}} - v_{\text{HI}}| \rangle = 14 \pm 11 \text{ km s}^{-1}$ (the error represents the 1σ dispersion). On average, larger velocity offsets between O VI and lower ions indicates that O VI does not necessarily trace the same phases of gas as the lower ions. On the other hand, SLFSs and pLLSs with no O VI are consistent with the gas being in a single phase.
3. We measure the velocity width, Δv_{90} , for HI, C II, C III, and O VI. The mean observed velocity width and dispersions are $\langle \Delta v_{90} \rangle = 82 \pm 22 \text{ km s}^{-1}$ for

HI, $74 \pm 27 \text{ km s}^{-1}$ for C II, $67 \pm 21 \text{ km s}^{-1}$ for C III, and $89 \pm 32 \text{ km s}^{-1}$ for O VI (the error represents the 1σ dispersion). HM O VI absorbers show larger mean velocity widths, $\Delta v_{90} = 92 \pm 31 \text{ km s}^{-1}$, compared with those of LM O VI absorbers, $\Delta v_{90} = 75 \pm 16 \text{ km s}^{-1}$. The higher line width of O VI in HM lower-ionization gas compared with LM lower-ionization gas suggests that HM SLFSs and pLLSs typically exhibit more pronounced multi-phase characteristics.

4. We observe a strong correlation between the O VI column density and metallicity, but not between O VI column density and HI column density. In particular, LM absorbers show weaker O VI absorption than HM absorbers, with mean (and uncertainty on the mean) values of $\log \langle N(\text{O VI}) \rangle = 13.46 \pm 0.02$ and 14.11 ± 0.01 , respectively, hinting at possible differences in the physical processes and origins of the O VI-bearing gas between these two populations.

With these findings, we group the SLFSs and pLLSs in three categories: (1) absorbers with non-detections of O VI with $\log N(\text{O VI}) < 13.6$; (2) absorbers with O VI detections with $\log N(\text{O VI}) \lesssim 14$; and (3) absorbers with O VI detections with $\log N(\text{O VI}) \gtrsim 14$. Comparing the distributions of the O VI and metallicity of the cool gas in surveys of O VI absorbers and galaxies (e.g., T22; Berg et al. (2023); S14; Johnson et al. 2015), we infer that:

1. SLFSs with no O VI are predominantly found in metal-poor ($[\text{X}/\text{H}] \leq -1.4$) gas and likely trace dense regions of the IGM.
2. SLFSs and pLLSs with O VI absorbers with $\log N(\text{O VI}) \lesssim 14$ are found at any metallicities and most likely probe dense IGM regions, extended CGM beyond R_{vir} .
3. SLFSs and pLLSs with O VI absorbers with $\log N(\text{O VI}) \gtrsim 14$ are mostly found in metal enriched gas ($[\text{X}/\text{H}] > -1.4$) and most likely probe the CGM within R_{vir} of star-forming galaxies. About 50% of these absorbers are also broad with $\Delta v_{90}(\text{O VI}) \gtrsim 100 \text{ km s}^{-1}$, which could be possibly signatures of active galaxy feedback.

Based on the above, we conclude that the combination of metallicity of the cool gas *and* O VI in surveys like CCC or KODIAQ provides a strong diagnostic of the origins of HI-selected absorbers and their association with galaxies. Further characterization of the galaxies in the fields of these absorbers would be extremely beneficial for a deeper understanding of the galaxies and their environments and use these absorbers as signatures of specific phenomena and environments.

Further knowledge on these absorbers can also be gained using cosmological simulations, as our entire

dataset is well suited to be modeled by a high-resolution cosmological simulation volume. For example, IllustrisTNG50 (Nelson et al. 2018; Pillepich et al. 2019), FIREbox (Feldmann et al. 2023), and E-MOSAICS (Pfeffer et al. 2018) provide ideal volumes to simulate both the IGM and CGM absorbers (see, e.g., the recent study by Weng et al. 2024 for HI absorbers at $z \sim 0.5$). By forward modeling COS sightlines using a mock sightline generator (e.g., Trident, Hummels et al. 2017), one can create full absorption systems, develop an algorithm to select HI-selected samples that mimic our pLLS/SLFS sample, and generate measurements of O VI column density, metallicity, velocity width, and velocity offsets between different ion species. This exercise would test whether the $N(\text{O VI})$ - $[\text{X}/\text{H}]$ correlation naturally arises in these simulations helping elucidate its origin. Moreover, it would provide additional insight into whether strong O VI in SLFSs/pLLSs arise from outflows and result in the observed velocity widths and offsets, and how that may depend on the impact parameter (e.g., Shen et al. 2013). Mallik et al. (2023); Mallik & Srikanand (2024); Maitra et al. (2024) using Sherwood simulations (Bolton et al. 2017) find that the statistical properties such as distribution functions of O VI column density, velocity spread, fraction of Ly α absorbers with detectable metal lines are influenced by feedback model implemented and the EUVB used. They find that changing the feedback model (for example, from stellar feedback only to a combination of stellar and active galactic nucleus feedback) can produce changes in the distribution functions that are comparable to those seen when varying the EUVB for a given feedback prescription.

ACKNOWLEDGEMENTS

We thank the referee for their detailed and helpful comments, which have strengthened and improved the manuscript. Support for this research was provided by NASA through grant HST-AR-15634 from the Space Telescope Science Institute (STScI), which is operated by the Association of Universities for Research in Astronomy, Incorporated, under NASA contract NAS5-26555. Data presented in this work were obtained from CCC, which was funded through NASA grant HST-AR-12854 from STScI. This research was supported by the Notre Dame Center for Research Computing through the Grid Engine software and the Notre Dame Cooperative Computing Lab through the HTCondor software. This research made use of

Software: Astropy (Astropy Collaboration et al. 2022), Matplotlib (Hunter 2007), PyIGM (Prochaska et al. 2017), NASA’s Astrophysics Data System (<https://>

//ui.adsabs.harvard.edu/), adstex (<https://github.com/yymao/adstex>).

Facilities: HST(COS)

REFERENCES

- Abel, G. J. 2015, *The R Journal*, 7, 15
- Akritas, M. G., Murphy, S. A., & Lavalley, M. P. 1995, *Journal of the American Statistical Association*, 90, 170
- Astropy Collaboration, Price-Whelan, A. M., Lim, P. L., et al. 2022, *ApJ*, 935, 167
- Barlow, R. 2003, in *Statistical Problems in Particle Physics, Astrophysics, and Cosmology*, ed. L. Lyons, R. Mount, & R. Reitmeyer, 250
- Berg, M. A., Lehner, N., Howk, J. C., et al. 2023, *ApJ*, 944, 101
- Bolton, J. S., Puchwein, E., Sijacki, D., et al. 2017, *MNRAS*, 464, 897
- Cameron, E. 2011, *PASA*, 28, 128
- Chen, H.-W., & Prochaska, J. X. 2000, *ApJL*, 543, L9
- Cooksey, K. L., Prochaska, J. X., Chen, H.-W., Mulchaey, J. S., & Weiner, B. J. 2008, *ApJ*, 676, 262
- Cooper, T. J., Simcoe, R. A., Cooksey, K. L., O’Meara, J. M., & Torrey, P. 2015, *ApJ*, 812, 58
- Cooper, T. J., Rudie, G. C., Chen, H.-W., et al. 2021, *MNRAS*, 508, 4359
- Crighton, N. H. M., Hennawi, J. F., & Prochaska, J. X. 2013, *ApJL*, 776, L18
- Crighton, N. H. M., Hennawi, J. F., Simcoe, R. A., et al. 2015, *MNRAS*, 446, 18
- Danforth, C. W., & Shull, J. M. 2005, *ApJ*, 624, 555
- Danforth, C. W., Keeney, B. A., Tilton, E. M., et al. 2016, *ApJ*, 817, 111
- Davé, R., Finlator, K., & Oppenheimer, B. D. 2012, *MNRAS*, 421, 98
- Dekel, A., & Birnboim, Y. 2006, *MNRAS*, 368, 2
- Epps, T., & Singleton, K. J. 1986, *Journal of Statistical Computation and Simulation*, 26, 177
- Faucher-Giguère, C.-A., Kereš, D., & Ma, C.-P. 2011, *MNRAS*, 417, 2982
- Feldmann, R., Quataert, E., Faucher-Giguère, C.-A., et al. 2023, *Monthly Notices of the Royal Astronomical Society*, 522, 3831
- Fox, A. J., Lehner, N., Tumlinson, J., et al. 2013, *ApJ*, 778, 187
- Fumagalli, M., O’Meara, J. M., & Prochaska, J. X. 2016, *MNRAS*, 455, 4100
- Fumagalli, M., Prochaska, J. X., Kasen, D., et al. 2011, *MNRAS*, 418, 1796
- Gibson, J. L., Lehner, N., Oppenheimer, B. D., et al. 2022, *AJ*, 164, 9
- Grimes, J. P., Heckman, T., Aloisi, A., et al. 2009, *ApJS*, 181, 272
- Hafen, Z., Faucher-Giguère, C.-A., Anglés-Alcázar, D., et al. 2017, *MNRAS*, 469, 2292
- Haislmaier, K. J., Tripp, T. M., Katz, N., et al. 2021, *MNRAS*, 502, 4993
- Heckman, T. M., Norman, C. A., Strickland, D. K., & Sembach, K. R. 2002, *ApJ*, 577, 691
- Hodges, J. L. 1958, *Arkiv for Matematik*, 3, 469
- Holland, S. T., et al. 2012, in *Cosmic Origins Spectrograph Instrument Handbook for Cycle 21 v. 5.0*, Vol. 5, 5
- Howk, J. C., Wotta, C. B., Berg, M. A., et al. 2017, *ApJ*, 846, 141
- Hummels, C. B., Smith, B. D., & Silvia, D. W. 2017, *ApJ*, 847, 59
- Hunter, J. D. 2007, *Computing in Science and Engineering*, 9, 90
- Johnson, S. D., Chen, H.-W., & Mulchaey, J. S. 2015, *MNRAS*, 449, 3263
- Johnson, S. D., Chen, H.-W., Mulchaey, J. S., Schaye, J., & Straka, L. A. 2017, *ApJL*, 850, L10
- Kacprzak, G. G., Churchill, C. W., Steidel, C. C., & Murphy, M. T. 2008, *AJ*, 135, 922
- Kacprzak, G. G., Churchill, C. W., Steidel, C. C., Spitler, L. R., & Holtzman, J. A. 2012, *MNRAS*, 427, 3029
- Kaplan, E. L., & Meier, P. 1958, *Journal of the American Statistical Association*, 53, 457
- Keeney, B. A., Stocke, J. T., Danforth, C. W., et al. 2017, *ApJS*, 230, 6
- Khaire, V., & Srianand, R. 2019, *MNRAS*, 484, 4174
- Lehner, N. 2017, in *Astrophysics and Space Science Library*, Vol. 430, *Gas Accretion onto Galaxies*, ed. A. Fox & R. Davé, 117
- Lehner, N., Howk, J. C., Marasco, A., & Fraternali, F. 2022a, *MNRAS*, 513, 3228
- Lehner, N., O’Meara, J. M., Fox, A. J., et al. 2014, *ApJ*, 788, 119
- Lehner, N., Prochaska, J. X., Kobulnicky, H. A., et al. 2009, *ApJ*, 694, 734
- Lehner, N., Wotta, C. B., Howk, J. C., et al. 2018, *ApJ*, 866, 33
- . 2019, *ApJ*, 887, 5
- Lehner, N., Howk, J. C., Tripp, T. M., et al. 2013, *ApJ*, 770, 138

- Lehner, N., Koppenhafer, C., O’Meara, J. M., et al. 2022b, *ApJ*, 936, 156
- Lofthouse, E. K., Fumagalli, M., Fossati, M., et al. 2020, *MNRAS*, 491, 2057
- . 2023, *MNRAS*, 518, 305
- Maitra, S., Mallik, S., & Srianand, R. 2024, *MNRAS*, 530, 3013
- Maller, A. H., & Bullock, J. S. 2004, *MNRAS*, 355, 694
- Mallik, S., & Srianand, R. 2024, *Monthly Notices of the Royal Astronomical Society*, 528, 3844
- Mallik, S., Srianand, R., Maitra, S., Gaikwad, P., & Khandai, N. 2023, *Monthly Notices of the Royal Astronomical Society*, 523, 2296
- Mandelker, N., van den Bosch, F. C., Springel, V., & van de Voort, F. 2019, *ApJL*, 881, L20
- Mandelker, N., van den Bosch, F. C., Springel, V., et al. 2021, *ApJ*, 923, 115
- Mann, H. B., & Whitney, D. R. 1947, *The Annals of Mathematical Statistics*, 18, 50
- Mantel, N., et al. 1966, *Cancer Chemother Rep*, 50, 163
- Marasco, A., Fraternali, F., Lehner, N., & Howk, J. C. 2022, *MNRAS*, 515, 4176
- Muzahid, S., Kacprzak, G. G., Churchill, C. W., et al. 2015, *ApJ*, 811, 132
- Nelson, D., Kauffmann, G., Pillepich, A., et al. 2018, *MNRAS*, 477, 450
- Oppenheimer, B. D., Davé, R., Katz, N., Kollmeier, J. A., & Weinberg, D. H. 2012, *MNRAS*, 420, 829
- Oppenheimer, B. D., Davé, R., Kereš, D., et al. 2010, *MNRAS*, 406, 2325
- Oppenheimer, B. D., Crain, R. A., Schaye, J., et al. 2016, *MNRAS*, 460, 2157
- Peeples, M., Tumlinson, J., Fox, A., et al. 2017, *The Hubble Spectroscopic Legacy Archive, Instrument Science Report COS 2017-4*, 8 pages, ,
- Péroux, C., & Howk, J. C. 2020, *ARA&A*, 58, 363
- Pfeffer, J., Kruijssen, J. M. D., Crain, R. A., & Bastian, N. 2018, *MNRAS*, 475, 4309
- Pillepich, A., Nelson, D., Springel, V., et al. 2019, *MNRAS*, 490, 3196
- Prochaska, J. X., & Wolfe, A. M. 1997, *ApJ*, 487, 73
- Prochaska, J. X., Tejos, N., cwotta, et al. 2017, *pygim/pygim: Initial release for publications, v.v1.0*, Zenodo, doi:10.5281/zenodo.1045480
- Qu, Z., Chen, H.-W., Rudie, G. C., et al. 2022, *MNRAS*, 516, 4882
- Qu, Z., Chen, H.-W., Johnson, S. D., et al. 2024, *ApJ*, 968, 8
- Rosenwasser, B., Muzahid, S., Charlton, J. C., et al. 2018, *MNRAS*, 476, 2258
- Sameer, Charlton, J. C., Norris, J. M., et al. 2021, *MNRAS*, 501, 2112
- Sameer, Charlton, J. C., Wakker, B. P., et al. 2024, *MNRAS*, 530, 3827
- Savage, B. D., Kim, T. S., Wakker, B. P., et al. 2014, *ApJS*, 212, 8
- Savage, B. D., Narayanan, A., Lehner, N., & Wakker, B. P. 2011, *ApJ*, 731, 14
- Savage, B. D., & Sembach, K. R. 1991, *ApJ*, 379, 245
- Schaye, J. 2001, *ApJ*, 559, 507
- Scholz, F. W., & Stephens, M. A. 1987, *Journal of the American Statistical Association*, 82, 918
- Sembach, K. R., Howk, J. C., Savage, B. D., Shull, J. M., & Oegerle, W. R. 2001, *ApJ*, 561, 573
- Shen, S., Madau, P., Guedes, J., et al. 2013, *ApJ*, 765, 89
- Shy, S., Tak, H., Feigelson, E. D., Timlin, J. D., & Babu, G. J. 2022, *AJ*, 164, 6
- Steidel, C. C., Pettini, M., & Hamilton, D. 1995, *AJ*, 110, 2519
- Stocke, J. T., Keeney, B. A., Danforth, C. W., et al. 2017, *ApJ*, 838, 37
- . 2013, *ApJ*, 763, 148
- . 2014, *ApJ*, 791, 128
- Suresh, J., Rubin, K. H. R., Kannan, R., et al. 2016, *Monthly Notices of the Royal Astronomical Society*, 465, 2966
- Tchernyshyov, K., Werk, J. K., Wilde, M. C., et al. 2022, *ApJ*, 927, 147
- . 2023, *ApJ*, 949, 41
- Thom, C., & Chen, H.-W. 2008a, *ApJS*, 179, 37
- . 2008b, *ApJ*, 683, 22
- Tripp, T. M., Sembach, K. R., Bowen, D. V., et al. 2008, *ApJS*, 177, 39
- Tripp, T. M., Meiring, J. D., Prochaska, J. X., et al. 2011, *Science*, 334, 952
- Tumlinson, J., Peeples, M. S., & Werk, J. K. 2017, *ARA&A*, 55, 389
- Tumlinson, J., Thom, C., Werk, J. K., et al. 2011, *Science*, 334, 948
- . 2013, *ApJ*, 777, 59
- Wakker, B. P., Savage, B. D., Sembach, K. R., Richter, P., & Fox, A. J. 2005, in *Astronomical Society of the Pacific Conference Series*, Vol. 331, *Extra-Planar Gas*, ed. R. Braun, 11
- Wallis, K. F. 2014, *arXiv e-prints*, arXiv:1405.4995
- Weng, S., Péroux, C., Ramesh, R., et al. 2024, *MNRAS*, 527, 3494
- Weng, S., Péroux, C., Karki, A., et al. 2023, *MNRAS*, 519, 931

- Werk, J. K., Prochaska, J. X., Thom, C., et al. 2012, *ApJS*, 198, 3
- Werk, J. K., Prochaska, J. X., Tumlinson, J., et al. 2014, *ApJ*, 792, 8
- Werk, J. K., Prochaska, J. X., Cantalupo, S., et al. 2016, *ApJ*, 833, 54
- Wilde, M. C., Werk, J. K., Burchett, J. N., et al. 2021, *ApJ*, 912, 9
- Wotta, C. B., Lehner, N., Howk, J. C., et al. 2019, *ApJ*, 872, 81
- Wotta, C. B., Lehner, N., Howk, J. C., O'Meara, J. M., & Prochaska, J. X. 2016, *ApJ*, 831, 95
- Zahedy, F. S., et al. 2019, *MNRAS*, 484, 2257

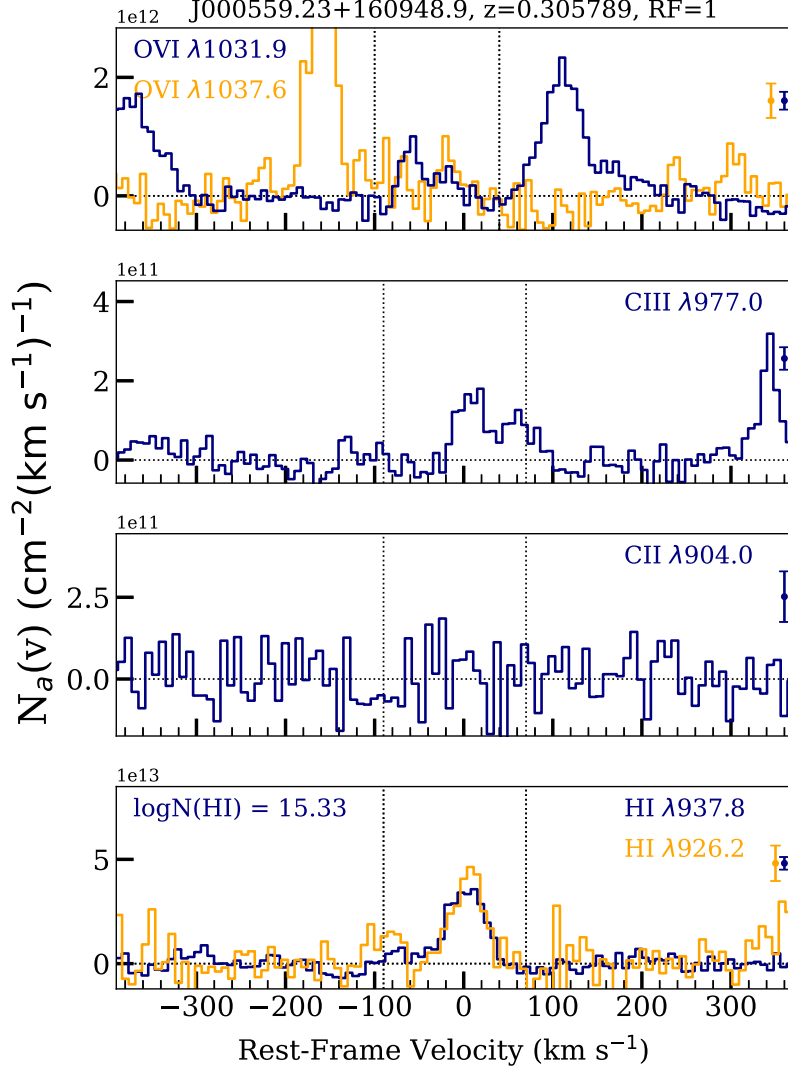


Figure 10. Apparent optical column density profiles for O VI, C II, C III, and H I, for the $z = 0.305789$ absorber toward the quasar J000559.23+160948.9. The integration velocity ranges are indicated by two vertical lines in each panel. The average symmetric uncertainty on the data is indicated to the right in each of the panels. The profiles are binned by 3 pixels for display purposes. The complete figure set (170 images) is available as supplementary material.

APPENDIX

We provide apparent column density, $N_a(v)$, profiles of O VI, C II, C III, and H I, as illustrated in Figure 10, for each absorber in this study (including those with lower S/N) as supplementary online material. These $N_a(v)$ plots include the adopted H I column densities from CCC I in the panel showing absorption in one of the weak H I transitions. We also provide normalized flux profiles of O VI, C II, C III, and H I for each absorber. Additional ions or transitions are available in CCC I. Figure 11 shows an example of these profiles. Vertical dashed lines in these figures indicate the velocity range encompassing the absorption, which was integrated to derive column densities and kinematics, including velocity and line-width. The complete set (170 images) of $N_a(v)$ and normalized flux profiles for the entire sample of O VI absorbers is provided as online supplementary material.

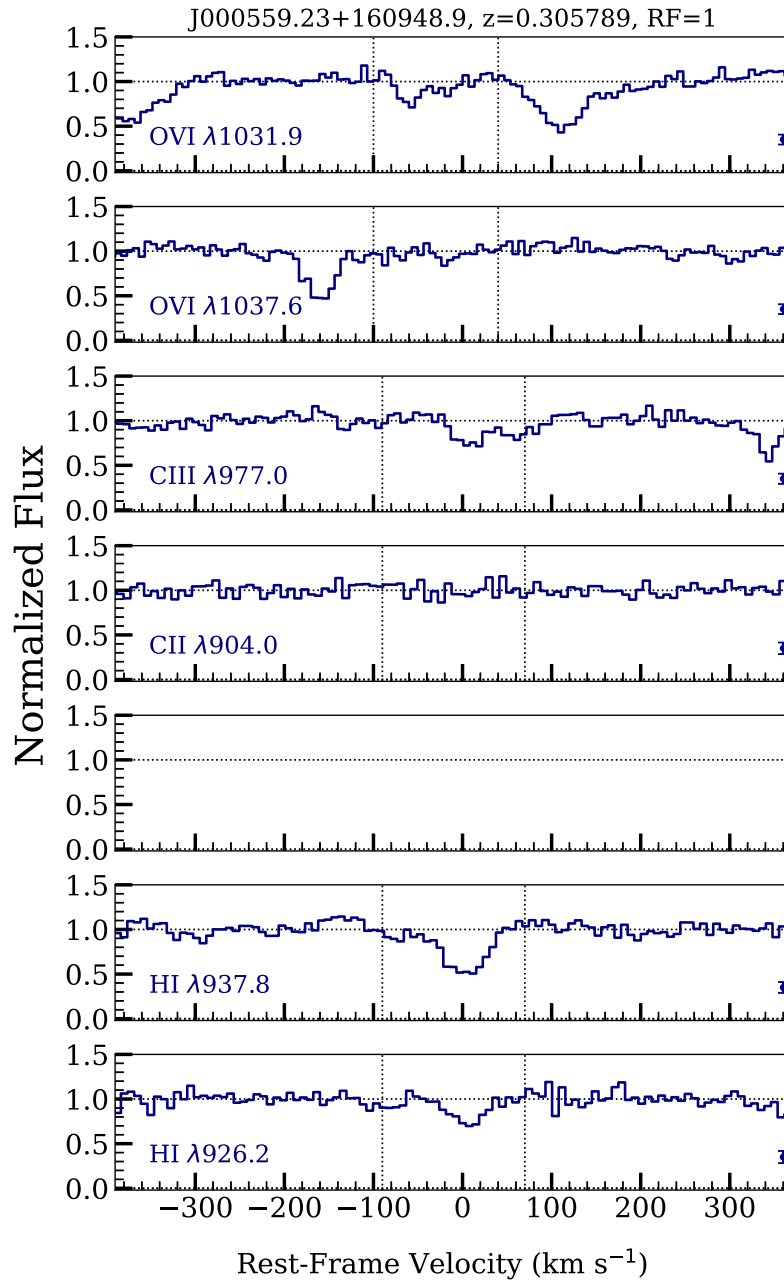


Figure 11. Normalized absorption lines of O VI, C II, C III, and H I, as a function of rest-frame velocity centered on the absorber at $z = 0.305789$ toward J000559.23+160948.9. These transitions are from COS G130M and G160M. The vertical dashed lines show the velocity range of the absorption over which the velocity profile was integrated to derive the column densities and kinematics. The average symmetric uncertainty on the data is indicated to the right in each of the panels. The profiles are binned by 3 pixels for display purposes. The complete figure set (170 images) is available as supplementary material.